THE TRANSMISSION CORRELATION IN THE Lyα FOREST PRODUCED BY RANDOMLY DISTRIBUTED LINES

Lin Zuo and J. Richard Bond
Canadian Institute for Theoretical Astrophysics, Toronto

May 1993; Submitted to the Ap. J.

48

ABSTRACT

The transmission of a quasar spectrum (flux divided by the continuum) is correlated because of the finite width of absorption lines. We describe a technique for calculating the transmission correlation function produced by randomly distributed lines. We also introduce an operationally straightforward procedure for measuring the pixel-pixel transmission correlation function ξ_{pp} directly from observed quasar spectra. We apply the method to 12 Sargent, Boksenberg & Steidel QSO spectra, and compare these with theoretical transmission correlation functions and with ξ_{pp} measured from computer-simulated quasar spectra of Lyα forest models with Poisson-distributed lines. The simulations are designed to mimic the observed spectrum as closely as possible, with the same wavelength sampling, instrumental resolution, continuum and noise properties. The comparisons with line distributions that are power laws in column density and redshift, and Gaussians in line width b reveal an excess in the observed ξ_{pp} at $\Delta v \simeq 150$ km s^{-1}, if we adopt the Carswell et al. (1991) parameters for the Gaussian (mean $b_0 = 30$ km s^{-1}, dispersion $\sigma_b = 10$ km s^{-1}). One possibility is that the Lyα forest lines are actually clustered at velocity separation scales $\Delta v \simeq 150$ km s^{-1}. Another possibility we explore here is that the b-distribution has more large b clouds and a larger dispersion. We find the observed ξ_{pp} is barely consistent with $b_0 = 40$ km s^{-1} and $\sigma_b = 25$ km s^{-1}. We show that the measured ξ_{pp} is relatively insensitive to the noise level and to errors in the continuum determination, unlike the traditional line counting methods, where the outcome is quite vulnerable to both. It also requires no line de-blending, and thus offers a powerful tool for extracting information from the crowded Lyα forest.

Subject headings: cosmology - quasars: absorption lines - intergalactic medium

1. INTRODUCTION

High redshift quasars show numerous narrow absorption lines at wavelengths shortward of Lyα emission when observed with relatively high spectral resolution. It is widely believed that most of the forest lines are Lyα absorption features which are produced by intervening absorbers (Lynds 1971; Sargent et al. 1980). Studies of Lyα absorption lines provide important information about the physical state and evolutionary history of intergalactic material at early epochs which is not accessible by other means.

To study the evolution of Lyα clouds, people have usually counted the number of absorption lines per unit redshift down to some apparent "rest equivalent width" limit above which the line list is deemed complete. However, because of the high density of absorption lines, especially at high redshift, the absorption lines are badly blended. As a routine de-blending procedure, observers use *straight line* cuts rather than the realistic line profiles to separate the blended absorption components, with the apparent "rest equivalent width" obtained by simply measuring the area within the cuts. (See Young et al. (1979), Carswell et al. (1982) and Hunstead et al. (1986) for detailed descriptions of line measurement.) It is clear that such apparent "rest equivalent widths" bear little relation to the intrinsic or physical rest equivalent widths of the absorption lines. Thus the "rest equivalent width" distribution derived from this data will depend upon the spectral resolution, since broad features observed at low resolution often break up into several narrower components at higher resolution, as shown vividly in Fig. 2 of Pettini et al. (1990).

A consequence of this is that if the value of the power law index γ — defined by the redshift evolution of the line number density through $d\mathcal{N}/dz \propto (1+z)^\gamma$ — is estimated using apparent "rest

equivalent widths", it will be sensitive to resolution. We call this apparent index γ_{app}. Because of the line-blending effect, γ_{app} also depends on the apparent "rest equivalent width" cut-off and the noise level in the QSO spectra. Using simulated quasar spectra with noise added, Liu & Jones (1988) have demonstrated that, for an input intrinsic $\gamma_{int} = 3.0$, the measured apparent $\gamma_{app} = 2.5 \pm 0.4$ for lines with an apparent "rest equivalent width" $W_{app} > 0.30\AA$, and $\gamma_{app} = 1.2 \pm 0.2$ for lines with $W_{app} > 0.15\AA$. This is easy to understand since the weak lines dominate the number counts and they are most vulnerable to the noise level in quasar spectra. It is interesting to note that the numerical simulations by Parnell & Carswell (1988) showed that the observed γ_{app} values tend to be only slightly below the input γ_{int}. However they only used one cut-off, $W_{app} = 0.32\AA$. Webb (1987), ran numerical simulations that showed it is only a lucky coincidence that $\gamma_{app} \simeq \gamma_{int}$ when the cut-off is chosen to be $0.32\AA$. Trevese et al. (1992) have reached the same conclusion.

One way to sidestep such uncertainties in the line counting statistics is to use D_A, the mean relative depression of the quasar continuum between Lyα and Lyβ emission, which was first introduced by Oke & Korycansky (1988). Its definition ensures that D_A is reasonably independent of instrumental resolution and, indeed, can be studied with much lower resolution data than that required for line counting statistics, but only *if* the true continuum level can be reliably extrapolated from the unabsorbed (red) region. Because it is operationally simple to measure D_A, this concept has since been applied by many many investigators (Bechtold et al. 1984; Steidel & Sargent 1987; O'Brien et al. 1988; Giallongo & Cristiani 1990; Jenkins & Ostriker 1991; Schneider, Schmidt & Gunn 1989a,b, 1991). In a recent paper, Zuo & Lu (1993) have measured D_A for a large sample of quasars. By extending the method proposed in Zuo (1993a) and Lu & Zuo (1993), they have used the measured D_A evolution with redshift to simultaneously estimate the intrinsic γ_{int} and the D_A normalization. Similar techniques, although differing in some important respects, have also been proposed by Press, Rybicki & Schneider (1993) and Press & Rybicki (1993) very recently.

Another way of doing statistics without counting lines was proposed by both Jenkins & Ostriker (1991) and Webb et al. (1992) (see also Press, Rybicki & Schneider 1993 and Press & Rybicki 1993). The technique is to use the pixel intensity (relative to an underlying continuum level) or transmission distribution over a specified wavelength interval to extract information from the Lyα forest.

Here, we introduce a new method to extract information from the Lyα forest. The idea is to calculate the transmission correlation produced by randomly distributed lines. The physics involved is very simple. Suppose we are counting photons in a detector wavelength bin which corresponds to the center wavelength of an absorption line. The count level is low in this wavelength bin of course. We are sure that in the nearby wavelength bins the counts are also low because these wavelength bins are part of the same absorption line, if the instrumental resolution is high enough to resolve the line. That is, the photon counts at two different wavelengths are correlated if the wavelength separation is less than a typical line width. Press, Rybicki & Schneider (1993) and Press & Rybicki (1993) have also explored the concept of correlations among neighboring spectral wavelength bins (we saw these two preprints after most part of the work presented here was completed), but the data they used were of very low spectral resolution (25Å) and cannot probe the velocity separation scales we are interested in here, since at such low resolution the absorption lines are not close to being resolved.

In this paper, we first use a simple analytic 'toy model' to illustrate the relationship between transmission correlation and intrinsic line widths (§2) if clouds come in only one type and then, in §3, we consider an ensemble of cloud types characterized by a power law distribution in column

density to derive a more realistic ensemble-averaged correlation function. In §4, we develop an operationally simple procedure for measuring the small scale transmission correlations produced by the resolved, but possibly blended, absorption lines directly from quasar spectra. We apply it to the high signal-to-noise ratio (S/N> 10) and relatively high spectral resolution (FWHM$\simeq 0.8\AA$) QSO spectra of Sargent, Boksenberg & Steidel (1989). In §5 and §6, we compare these measurements with the theoretical predictions of §3 and measurements made from computer-simulated quasar spectra of Poisson-distributed lines with power law distributions in column density, redshift and Gaussian distributions in line width. We summarize our basic results in §7.

2. AN ILLUSTRATIVE TOY MODEL

In this section, we illustrate the sort of features one expects in transmission correlation functions using a simple analytic model consisting of identical Poisson-distributed clouds with 'top hat' optical depth profiles of depth τ_0 and width δv (§2.1). We also show the modifications that result when finite instrumental resolution, modelled in this section by a top hat' of width v_I, is included (§2.2). The results are shown in Fig.1(a,b,c).

2.1 Infinite Spectral Resolution Case

Consider the following simple toy model which captures the essence of the problem we are facing. We suppose that, on average, there are m identical absorbing clouds along the line of sight. We ignore evolution effects (*i.e.*, our calculations are carried out in Euclidean space). The position of an absorbing cloud along the line-of-sight is characterized by a velocity v_c related to the observed wavelength by $\lambda_{obs} \propto v_c$ (non-relativistic velocity is assumed throughout this section). We assume the distribution function of the clouds, $f(v_c)$, is a top hat over some (large) range in velocity

$$f(v_c) = \begin{cases} \frac{1}{v_f} & \text{if } v_l < v_c < v_u \equiv v_l + v_f \\ 0 & \text{otherwise} \end{cases} . \tag{2.1}$$

Each cloud has an optical depth, which we denote by $\tau_c(v)$. We adopt a top hat profile for the depth about the line center,

$$\tau_c(v - v_c) = \begin{cases} \tau_0 & \text{if } -\delta v/2 < v - v_c < \delta v/2 \\ 0 & \text{otherwise.} \end{cases} \tag{2.2}$$

We require that $v_f \gg \delta v$.

We denote the total optical depth at v produced by all the clouds along the line of sight by $\tau(v)$. We call $e^{-\tau(v)}$ the transmission at v. In the case considered here of Poisson-distributed clouds, the effective optical depth $\tau_{eff}(v)$, defined through the mean transmission by $e^{-\tau_{eff}} \equiv \langle e^{-\tau} \rangle$ (Zuo & Phinney 1993), is given by

$$\tau_{eff}(v) = \begin{cases} 0 & \text{if } v < v_l - \frac{\delta v}{2} \\ \frac{m}{v_f}(1 - e^{-\tau_0})(\delta v/2 + v - v_l) & \text{if } v_l - \frac{\delta v}{2} < v < v_l + \frac{\delta v}{2} \\ \frac{m}{v_f}(1 - e^{-\tau_0})\delta v & \text{if } v_l + \frac{\delta v}{2} < v < v_u - \frac{\delta v}{2} \\ \frac{m}{v_f}(1 - e^{-\tau_0})(\delta v/2 + v_u - v) & \text{if } v_u - \frac{\delta v}{2} < v < v_u + \frac{\delta v}{2} \\ 0 & \text{if } v > v_u + \frac{\delta v}{2}. \end{cases} \tag{2.3}$$

There is an edge effect near the v_l and v_u boundaries since clouds moving with $v \lesssim v_u$ and $v \gtrsim v_l$ can absorb at $v > v_u$ and $v < v_l$ because of the finite width δv of the absorption profile. Since we are only interested in the case in which $v_f \gg \delta v$, we can neglect the edge effect. Thus $\tau_{eff}(v)$ is a constant independent of v in the range between v_l and v_u.

The mean optical depth $\langle\tau(v)\rangle$ can also be calculated using Poisson statistics:

$$\langle\tau(v)\rangle = \sum_{k=0}^{\infty} \frac{k\tau_0\delta v}{v_f} e^{-m}\frac{m^k}{k!} = \frac{m\tau_0\delta v}{v_f} \equiv N_l\tau_0 \quad \text{for} \quad v_l < v < v_u \ , \tag{2.4}$$

where $N_l = m\delta v/v_f$ is the mean number of lines in the velocity interval δv. When $\tau_0 \ll 1$, we have $\tau_{eff}(v) \simeq \langle\tau(v)\rangle$.

The total optical depth is actually discrete in our case, an integer multiple of τ_0. It is easy to show that, at a point v in the spectrum, with $v_l < v < v_u$, the probability that the depth is zero is

$$p(\tau = 0) = e^{-m\delta v/v_f} \tag{2.5}$$

and the probability that it is τ_0 is

$$p(\tau = \tau_0) = \frac{\frac{\delta v}{v_f}}{\left(1 - \frac{\delta v}{v_f}\right)}\left(e^{-m\delta v/v_f} - e^{-m}\right). \tag{2.6}$$

We now derive the transmission correlation function, $\xi_0(\Delta v)$, a function of the velocity difference $\Delta v \equiv v_2 - v_1$ between velocity pairs, for this model. It is defined by

$$1 + \xi_0(\Delta v) \equiv \frac{\langle e^{-\tau(v_1)}e^{-\tau(v_2)}\rangle}{e^{-\tau_{eff}(v_1)}e^{-\tau_{eff}(v_2)}} = \frac{\langle F(v_1)F(v_2)\rangle}{\langle F(v_1)\rangle\langle F(v_2)\rangle} \ , \tag{2.7}$$

The observed flux is related to the transmission function $e^{-\tau(v)}$ and the 'continuum level' of the spectrum, F_0, by $F(v) = F_0 e^{-\tau(v)}$. For simplicity, we assume F_0 is independent of v.

Zuo & Phinney (1993) show that

$$\langle e^{-\tau(v_1)}e^{-\tau(v_2)}\rangle = e^{-II(v_1,v_2)} \ , \tag{2.8a}$$

where

$$II(v_1, v_2) = m\int_{v_l}^{v_u} f(v')\left[1 - e^{-\tau_c(v'-v_1)}e^{-\tau_c(v'-v_2)}\right] dv' \ , \tag{2.8b}$$

which, for the toy model, reduces to

$$II(v_1, v_2) = \begin{cases} \frac{2m}{v_f}\left(1 - e^{-\tau_0}\right)|\Delta v| & \\ \quad + \frac{m}{v_f}\left(1 - e^{-2\tau_0}\right)(\delta v - |\Delta v|) & \text{if } |\Delta v| < \delta v \\ \frac{2m\delta v}{v_f}\left(1 - e^{-\tau_0}\right) & \text{if } |\Delta v| > \delta v. \end{cases} \tag{2.8c}$$

Combining eq.(2.3) with this gives a simple expression for the transmission correlation function,

$$1 + \xi_0(\Delta v) = \begin{cases} \exp[N_l(1 - |\Delta v|/\delta v)(1 - e^{-\tau_0})^2] & \text{if } 0 \le |\Delta v|/\delta v < \delta v \\ 1 & \text{if } |\Delta v|/\delta v > 1. \end{cases} \tag{2.9}$$

2.2 Finite Instrumental Resolution Effect

So far we have assumed infinite spectral resolution. We now examine the effects caused by finite instrumental resolution. Suppose that the instrumental response function is given by a top hat of width $v_{\mathcal{I}}$,

$$\mathcal{I}(v) = \begin{cases} \frac{1}{v_{\mathcal{I}}} & \text{if } -v_{\mathcal{I}}/2 < v < v_{\mathcal{I}}/2 \\ 0 & \text{otherwise.} \end{cases} \tag{2.10}$$

We assume the width is small compared with the v-interval over which the clouds exist, *i.e.*, $v_{\mathcal{I}} \ll v_f$. After convolving with this instrumental profile, the square profile of an absorption line becomes trapezoidal.

For an intrinsic flux $F(v)$, the observed apparent flux is given by

$$F_{\mathcal{I}}(v) = \int_{-\infty}^{\infty} \mathcal{I}(v-v')F(v')dv' = \int_{-\infty}^{\infty} \mathcal{I}(v-v')F_0 e^{-\tau(v')}dv' \ . \tag{2.11}$$

We wish to calculate the flux correlation function, defined by

$$1 + \xi(\Delta v) \equiv \frac{\langle F_{\mathcal{I}}(v_1)F_{\mathcal{I}}(v_2)\rangle}{\langle F_{\mathcal{I}}(v_1)\rangle\langle F_{\mathcal{I}}(v_2)\rangle} \ . \tag{2.12}$$

The form chosen for $\mathcal{I}(v)$ leads to $\langle F_{\mathcal{I}}(v)\rangle = F_0 e^{-\tau_{eff}(v)}$ and

$$\langle F_{\mathcal{I}}(v_1)F_{\mathcal{I}}(v_2)\rangle = \frac{F_0^2}{v_{\mathcal{I}}^2}\int_{v_1-v_{\mathcal{I}}/2}^{v_1+v_{\mathcal{I}}/2} dv_1' \int_{v_2-v_{\mathcal{I}}/2}^{v_2+v_{\mathcal{I}}/2} dv_2' e^{-II(v_1',v_2')} \ .$$

To simplify the integration, we introduce a new coordinate system (x', y'), which is obtained by first shifting the old coordinate system origin to $(v_1', v_2') = (v_1 - v_{\mathcal{I}}/2, v_2 - v_{\mathcal{I}}/2)$ and then rotating it clockwise by an angle of $\pi/4$. The new coordinates are thus related to the old ones by

$$\begin{cases} x' = \frac{1}{\sqrt{2}}(v_1' - v_2' + v_2 - v_1), \\ y' = \frac{1}{\sqrt{2}}(v_1' + v_2' - v_1 - v_2 + v_{\mathcal{I}}) \ . \end{cases}$$

We then get

$$\begin{aligned} \langle F_{\mathcal{I}}(v_1)F_{\mathcal{I}}(v_2)\rangle = & \frac{F_0^2}{v_{\mathcal{I}}^2}\int_{-v_{\mathcal{I}}/\sqrt{2}}^{0} (2x' + \sqrt{2}v_{\mathcal{I}})e^{-II(v_1',v_2')}dx' \\ & + \frac{F_0^2}{v_{\mathcal{I}}^2}\int_{0}^{v_{\mathcal{I}}/\sqrt{2}} (-2x' + \sqrt{2}v_{\mathcal{I}})e^{-II(v_1',v_2')}dx'. \end{aligned}$$

We denote the ratio of instrumental resolution width to intrinsic line width by $y_{\mathcal{I}} \equiv v_{\mathcal{I}}/\delta v$. We also let $y \equiv |\Delta v|/\delta v$. Then for $y > 1 + y_{\mathcal{I}}$ we have $\xi(\Delta v) = 0$, while for $y < 1 + y_{\mathcal{I}}$ we have

$$1 + \xi(\Delta v) = \frac{\exp[N_l(1-e^{-\tau_0})^2]}{y_{\mathcal{I}}^2}\int_0^{y_{\mathcal{I}}} (-u + y_{\mathcal{I}})\left(e^{-g(y,u)} + e^{-h(y,u)}\right) du, \tag{2.13a}$$

where

$$g(y,u) = \begin{cases} N_l(1-e^{-\tau_0})^2|y-u| & \text{if } |y-u|<1 \\ N_l(1-e^{-\tau_0})^2 & \text{if } |y-u|>1 \end{cases} \tag{2.13b}$$

and

$$h(y,u) = \begin{cases} N_l(1-e^{-\tau_0})^2(y+u) & \text{if } (y+u)<1 \\ N_l(1-e^{-\tau_0})^2 & \text{if } (y+u)>1. \end{cases} \tag{2.13c}$$

For given N_l, τ_0 and $y_{\mathcal{I}}$, analytic expressions for $\xi(\Delta v)$ as a function y can be obtained easily. Our calculated results are plotted in Figs. 1(a), (b) and (c). As expected, increasing $y_{\mathcal{I}}$ decreases $\xi(\Delta v)$ for small $\Delta v/\delta v$ values, but there is a compensating increase at large $\Delta v/\delta v$. Figs. 1(b,c) also show that, for given $\langle\tau\rangle = N_l\tau_0$, larger τ_0 leads to larger $\xi(\Delta v)$.

3. TRANSMISSION CORRELATION IN THE Lyα FOREST

In this section, we calculate the transmission correlation function for uncorrelated absorption lines distributed according to the conventional power-law form for $\eta(z,N)dzdN$,

$$\eta(z,N) = A(1+z)^{\gamma_{int}}N^{-\beta}\ , \quad N_l < N < N_u\ .$$

where η is the mean number of absorbing clouds along the line of sight in the redshift interval $z \to z+dz$ with an HI column density in the range $N \to N+dN$. For simplicity, we also assume that the velocity-spread parameter b is the same for all Lyα clouds and does not evolve with redshift. We consider the influence of a Gaussian spread in §5.

3.1 Infinite Spectral Resolution Case

We now derive the transmission correlation produced by randomly distributed Lyα forest lines for the case of no instrumental degradation of the resolution. Our calculations are now necessarily carried out for an expanding universe. Assume that the line-of-sight to a quasar of redshift z_{em} we observe passes through a smoothly distributed intergalactic medium (IGM) and some randomly distributed discrete absorbing clouds. At the observed wavelength λ_1, the smooth IGM produces a 'Gunn-Peterson' optical depth $\tau_{GP}(\lambda_1)$ and the clouds contribute an optical depth $\tau(\lambda_1)$. The observed flux is then given by $F(\lambda_1) = F_0(\lambda_1)e^{-\tau_{GP}(\lambda_1)}e^{-\tau(\lambda_1)}$, where F_0 would be the observed flux if there were no absorption. Now consider a close pair of observed wavelengths λ_1 and λ_2, which have a separation less than several typical observed absorption line widths. We define $\lambda_c \equiv (\lambda_1+\lambda_2)/2$ and its corresponding redshift $z_c \equiv (\lambda_c/\lambda_\alpha)-1$, where λ_α is the rest-frame Lyα wavelength. The relative velocity of two clouds corresponding to λ_1 and λ_2 is $\Delta v = c|\lambda_2-\lambda_1|/\lambda_c$. The transmission correlation function at z_c is defined by

$$1+\xi_0(\Delta v) \equiv \frac{\langle e^{-\tau(\lambda_1)}e^{-\tau(\lambda_2)}\rangle}{e^{-\tau_{eff}(\lambda_1)}e^{-\tau_{eff}(\lambda_2)}} = \frac{\langle F(\lambda_1)F(\lambda_2)\rangle}{\langle F(\lambda_1)\rangle\langle F(\lambda_2)\rangle}\ , \tag{3.1}$$

where τ_{eff} is the effective optical depth produced by randomly distributed discrete clouds (see Zuo & Phinney 1993).

Assuming Poisson-distributed lines distributed according to the probability density $\eta(z,N) = A(1+z)^{\gamma_{int}}N^{-\beta}$, Zuo & Phinney (1993) showed that

$$\tau_{eff}(0,z_{em},\lambda_1) \simeq \tau_{eff}(0,z_{em},\lambda_2) \simeq \tau_{eff}(\lambda_c) = \frac{A(1+z_c)^{\gamma_{int}+1}}{\lambda_\alpha}\int_{N_l}^{N_u} N^{-\beta}W_{res}(N,b)dN\ , \tag{3.2}$$

where b is the (single non-evolving) velocity-spread parameter and $W_{res}(N,b)$ is the rest equivalent width of an absorption line and N_l and N_u are the lower and upper HI column density limits, respectively. Zuo & Phinney (1993) also showed that the correlation,

$$e^{-II(\lambda_1,\lambda_2)} \equiv \langle e^{-\tau(\lambda_1)} e^{-\tau(\lambda_2)} \rangle \ , \tag{3.3a}$$

is given by

$$II(\lambda_1,\lambda_2) = A \int_{N_l}^{N_u} N^{-\beta} dN \int_0^{z_{em}} (1+z)^{\gamma_{int}} \left[1 - e^{-\tau_c(\lambda_{1z},N,b)} e^{-\tau_c(\lambda_{2z},N,b)}\right] dz \ . \tag{3.3b}$$

Here, τ_c is the optical depth produced by a single cloud and $\lambda_{1z} = \lambda_1/(1+z)$ and $\lambda_{2z} = \lambda_2/(1+z)$. When the wavelength separation is large, we have $II(\lambda_1,\lambda_2) \simeq 2\tau_{eff}(\lambda_c)$. In specific calculations given in this section, we shall assume that the line profile is entirely determined by Doppler broadening and that the velocity distribution within an absorbing cloud is Maxwellian. We thus have

$$W_{res}(N,b) = \frac{2b\lambda_\alpha}{c} \int_0^\infty \left[1 - \exp[-\tau_0 e^{-u^2}]\right] du \tag{3.4}$$

and

$$II(\lambda_1,\lambda_2) \simeq 2A(1+z_c)^{\gamma_{int}+1} \left(\frac{b}{c}\right) \times \int_{N_l}^{N_u} N^{-\beta} dN \int_0^\infty \left[1 - \exp[-\tau_0 \left[e^{-[u-\Delta v/(2b)]^2} + e^{-[u+\Delta v/(2b)]^2}\right]\right] du \ , \tag{3.5}$$

where $\tau_0 = aN$, with $a = 7.574 \times 10^{-13}/[b/(\mathrm{km\,sec}^{-1})]$ denoting the Lyα line center optical depth (Spitzer 1978). We also have, for small wavelength separations,

$$e^{-\tau_{eff}(\lambda_1)} e^{-\tau_{eff}(\lambda_2)} \simeq e^{-2\tau_{eff}(\lambda_c)} \ . \tag{3.6}$$

All of the ingredients necessary for the calculation of the transmission correlation function are now in place.

In Figs. 2(a), (b) and (c), we plot $1 + \xi_0(\Delta v)$ as a function of $\Delta v/b$ for various given redshifts z_c and for several models, denoted by DB1 to DB7, in which we vary the parameters defining the line-distribution, as listed in Table 1. We have normalized the line distribution $\eta(z,N)$ by requiring that it reproduces the observed $D_A = 0.2$ for a $z_{em} = 2.875$ quasar. This determines A in $\eta(z,N)$ (Zuo 1993a; see also Section 5 below for more details). These figures show that $\xi_0(\Delta v)$ is sensitive to the input γ_{int} and β values and that it increases very rapidly with increasing redshift. The large magnitude of the transmission correlation function at small velocity separations is unavoidable and we shall see in the next section that it is indeed there in the data.

The weak line limit, $aN_u \ll 1$, has a simple form,

$$1 + \xi_0(\Delta v) \simeq \exp[I_W(\Delta v/b)] \ , \tag{3.7a}$$

where

$$I_W(\Delta v/b) = \frac{Aa^2}{3-\beta}\sqrt{\frac{\pi}{2}} \left(\frac{b}{c}\right) (1+z_c)^{\gamma_{int}+1} e^{-(\Delta v/b)^2/2} \left[N_u^{3-\beta} - N_l^{3-\beta}\right] . \tag{3.7b}$$

An interesting strategy is suggested, that we chop out the strong lines from Lyα forests and study the transmission correlation produced only by weak lines.

3.2 Finite Instrumental Resolution Effect

Now consider the situation in which our instrumental response function is not infinitely narrow but is given by $\mathcal{I}(\lambda)$. For an incoming flux $F(\lambda)$ in front of the telescope at the observed wavelength λ, the observed apparent flux is given by

$$\begin{aligned} F_{\mathcal{I}}(\lambda) &= \int_{-\infty}^{\infty} \mathcal{I}(\lambda-\lambda')F(\lambda')d\lambda' = \int_{-\infty}^{\infty} \mathcal{I}(\lambda-\lambda')F_0(\lambda')e^{-\tau_{GP}(\lambda')}e^{-\tau(\lambda')}d\lambda' \\ &\simeq F_0(\lambda)e^{-\tau_{GP}(\lambda)} \int_{-\infty}^{\infty} \mathcal{I}(\lambda-\lambda')e^{-\tau(\lambda')}d\lambda'. \end{aligned} \tag{3.8}$$

If we assume that the width of the instrument profile is not very much larger than the typical absorption line width b, we then have

$$\begin{aligned} \langle F_{\mathcal{I}}(\lambda_1)\rangle\langle F_{\mathcal{I}}(\lambda_2)\rangle &\simeq \langle F(\lambda_1)\rangle\langle F(\lambda_2)\rangle \\ &\simeq F_0(\lambda_1)F_0(\lambda_2)e^{-\tau_{GP}(\lambda_1)}e^{-\tau_{GP}(\lambda_2)}e^{-2\tau_{eff}(\lambda_c)} \end{aligned}$$

and

$$\begin{aligned} \langle F_{\mathcal{I}}(\lambda_1)F_{\mathcal{I}}(\lambda_2)\rangle \simeq F_0(\lambda_1)F_0(\lambda_2)e^{-\tau_{GP}(\lambda_1)}e^{-\tau_{GP}(\lambda_2)} \times \\ \int_{-\infty}^{\infty} d\lambda_1' \int_{-\infty}^{\infty} d\lambda_2' \mathcal{I}(\lambda_1-\lambda_1')\mathcal{I}(\lambda_2-\lambda_2')\langle e^{-\tau(\lambda_1')}e^{-\tau(\lambda_2')}\rangle \ . \end{aligned}$$

Introducing a line transmission factor

$$T(\lambda) \equiv \frac{F_{\mathcal{I}}(\lambda)}{F_0(\lambda)e^{-\tau_{GP}(\lambda)}} \ , \tag{3.9}$$

we define the (instrument-degraded) transmission correlation function $\xi(\Delta v)$ to be

$$1+\xi(\Delta v) \equiv \frac{\langle T(\lambda_1)T(\lambda_2)\rangle}{\langle T(\lambda_1)\rangle\langle T(\lambda_2)\rangle} = \frac{\langle F_{\mathcal{I}}(\lambda_1)F_{\mathcal{I}}(\lambda_2)\rangle}{\langle F_{\mathcal{I}}(\lambda_1)\rangle\langle F_{\mathcal{I}}(\lambda_2)\rangle}. \tag{3.10}$$

We now adopt a Gaussian form of width σ_λ for the instrumental profile:

$$\mathcal{I}(\lambda) = \frac{1}{\sigma_\lambda\sqrt{2\pi}} \exp[-\frac{\lambda^2}{2\sigma_\lambda^2}] \ . \tag{3.11}$$

Since $\langle e^{-\tau(\lambda_1')}e^{-\tau(\lambda_2')}\rangle$ depends only on $(\lambda_1'-\lambda_2')$ in our approximation, we introduce a new coordinate system (λ_+', λ_-'):

$$\begin{cases} \lambda_+' = (\lambda_1'+\lambda_2')/2 \ , \\ \lambda_-' = \lambda_1'-\lambda_2' \ . \end{cases}$$

We then have

$$\int_{-\infty}^{\infty} d\lambda_1' \int_{-\infty}^{\infty} d\lambda_2' \mathcal{I}(\lambda_1 - \lambda_1')\mathcal{I}(\lambda_2 - \lambda_2')\langle e^{-\tau(\lambda_1')} e^{-\tau(\lambda_2')}\rangle$$

$$= \frac{1}{\sigma_\lambda 2\sqrt{\pi}} \int_{-\infty}^{\infty} d\lambda_-' e^{-\frac{[\lambda_-' - \lambda_a(1+z_c)\Delta v/c]^2}{4\sigma_\lambda^2}} \langle e^{-\tau(\lambda_1')} e^{-\tau(\lambda_2')}\rangle$$

$$= \frac{1}{\sigma'\sqrt{2\pi}} \int_{-\infty}^{\infty} d\zeta e^{-\frac{(\zeta - \Delta v/b)^2}{2\sigma'^2}} \langle e^{-\tau(\lambda_1')} e^{-\tau(\lambda_2')}\rangle \ ,$$

where $\sigma' = \sqrt{2}c\sigma_\lambda/(\lambda_c b)$ and $\zeta = c\lambda_-'/(\lambda_c b)$. It is now straightforward to get

$$1 + \xi(\Delta v) = \frac{1}{\sigma'\sqrt{2\pi}} \int_0^{\infty} d\zeta \left(\exp[-\frac{(\zeta - \Delta v/b)^2}{2\sigma'^2}] + \exp[-\frac{(\zeta + \Delta v/b)^2}{2\sigma'^2}] \right) [1 + \xi_0(\zeta)] \ . \qquad (3.12)$$

In Fig. 4(d), we show the effect of varying the instrumental resolution σ_λ on the Model DB1 transmission correlation function. The FWHM is related to σ_λ by FWHM$=2\sigma_\lambda\sqrt{2\ln 2}$. Just as for the toy models of the previous section, we see that low resolution (large σ_λ) decreases the correlation at small velocity separations and has a long compensating tail at large velocity separations.

4. MEASUREMENTS OF QSO PIXEL-PIXEL TRANSMISSION CORRELATION

4.1 QSO Sample Used in This Work

There exists a large number of QSO spectra observed at resolution 0.8—1.5Å with relatively high signal-to-noise ratio. Although spectra at this resolution are not useful for fitting line profiles to get the HI column density N and the Doppler width b, they do provide a useful data base for the transmission correlation analysis, as we now show.

We have measured the pixel-pixel transmission correlations for 12 quasars. These quasars are taken from the published CIV survey sample of Sargent, Boksenberg & Steidel (1988). The Lyα forest regions of these quasars are observed with a spectral resolution either 0.8 or 1.5Å (FWHM). The signal-to noise ratio, S/N, is usually larger than 15. The names of the QSOs and their emission redshifts are listed in Table 2. The details of the observations can be found in Sargent, Boksenberg & Steidel (1988). We are grateful to Dr. Wal Sargent for allowing us to use the spectra in digital form. Dr. Limin Lu kindly provided us with the continuum fits. The data arrays give the wavelengths, the relative intensities and the fitted continuum levels for all pixels. In Fig. 3, we show one of these spectra and its continuum fit, that of QSO 0837+109.

4.2 Measuring the Pixel-pixel Transmission Correlation Function ξ_{pp}

There are $N_p(N_p - 1)/2$ wavelength pairs for a quasar spectrum with N_p pixels. We are here mainly interested in small velocity separations with wavelength differences not very much larger than several typical line widths. Thus the velocity separation corresponding to the observed wavelengths λ_1 and λ_2 can be calculated by $\Delta v = 2c|\lambda_2 - \lambda_1|/(\lambda_1 + \lambda_2)$. After calculating Δv for the pixel pairs we are interested in, we group the pairs into many velocity bins. We estimate $e^{-\tau_{eff}}$ by

$$e^{-\tau_{eff}} \simeq DB \equiv \frac{\sum_{i=1}^{N_p} F_i/F_{C_i}}{N_p} \ , \qquad (4.1)$$

where N_p is the total number of pixels in the wavelength range we are interested in and F_i and F_{C_i} are the observed flux level and the fitted continuum level in the ith pixel, respectively. We also estimate the covariance function for the transmission factor for the velocity separation Δv_j by

$$\langle T(\lambda_1)T(\lambda_2)\rangle_{\Delta v_j} \simeq DU_j \equiv \frac{\sum_{k=1}^{N_j}\left[\left(\frac{F}{F_C}\right)_1 \times \left(\frac{F}{F_C}\right)_2\right]_{jk}}{N_j} , \tag{4.2}$$

where N_j is the total number of velocity separation pairs in the jth velocity bin, $[(F/F_C)_1(F/F_C)_2]_{jk}$ is the contribution from the kth pair in this Δv_j bin, and the subscripts 1 and 2 denote the first and the second component of the pair, respectively. We then define the pixel-pixel transmission correlation at separation Δv_j by

$$1 + \xi_{pp}(\Delta v_j) \equiv \frac{DU_j}{(DB)^2} , \tag{4.3}$$

where Δv_j is the mean velocity separation of the pixel pairs in the jth velocity bin. By this definition, we expect that the theoretical $1 + \xi(\Delta v_j)$ in eq.(3.12) is roughly $1 + \xi_{pp}(\Delta v_j)$. Our measured results for the 12 quasars are shown in Figs. 4(a) and (b); each figure contains six curves with comparable spectral resolution. The observed wavelength range used in the transmission correlation measurement is listed in Table 2 for each QSO in our sample. Notice that for Q2206-199, we have cut the spectrum at $\lambda_{obs} = 3820\AA$ to avoid the strong damped Lyα trough at $\lambda_{obs} \simeq 3743\AA$.

In Table 2 the object names are in the first column, the emission redshifts in the second column and the third column shows the spectral resolution. Notice that Q1159+124 and Q1623+269 have been observed with different resolutions in the Lyα forest regions. The fourth column lists the observed wavelength ranges. We have chosen the two limiting wavelengths to include only those pixels between the Lyα and Lyβ emissions and to exclude some identified absorption lines at the two ends, but have not excluded the identified lines within the wavelength range. The total number of lines and the identified lines (associated with metal line systems) within the λ_{obs} range are given in the last column for each QSO. These lines are listed in Sargent, Boksenberg & Steidel (1988).

The measured transmission correlation function depends somewhat upon the choice for the velocity bins. Sargent, Boksenberg & Steidel rebinned their data to logarithmic scales, with each pixel corresponding to a constant velocity spread (with a few exceptions). This binning is therefore a natural one for us to adopt. So for quasar spectral data in this form with N_p pixels, we proceed as follows: we calculate all the velocity separations for the wavelength pairs we are interested in, sort these velocity pairs in ascending order, then take the first $(N_p - 1)$ pairs as our first (smallest) velocity bin, the next $N_p - 2$ pairs as the second velocity bin, and so on. If N_p is large, a large number of pixel pairs contribute to each small-velocity separation bin.

Figs. 4(a,b) show the $1 + \xi_{pp}$ curves become noisy at velocity separations $\Delta v > 200$ km s^{-1}. Below $\Delta v \simeq 200$ km s^{-1}, we have consistent transmission correlation signals displaying the expected trend that higher z_{em} quasars have higher ξ_{pp} (an exception is Q0424–131). This suggests that the fluctuations in ξ_{pp} are relatively small at $\Delta v < 200$ km s^{-1}, and we can reasonably use results for individual quasars with which to compare our theoretical model predictions.

4.3 Comparison with Theoretical Predictions

Our procedure for measuring ξ_{pp} has contributions from absorption lines of varying redshifts, and thus it cannot be directly compared with the transmission correlation functions calculated in the last section. However, we do expect that ξ_{pp} should lie between the theoretical ξ curves of eq.(3.12) calculated for z_{min} and z_{max}, where z_{min} corresponds to the first pixel and z_{max} to the last pixel of the wavelength range used in the measurement of ξ_{pp}. For a high z_{em} quasar, z_{min} differs significantly from z_{max} (which is usually z_{em}) if we use most of the spectrum between Lyβ and Lyα emission. Because the flux correlation function increases rapidly with increasing redshift, it is best to use Monte Carlo simulations of quasar spectra and measure them in the way we do for the real quasar to constrain input model parameters. We do this in §5.

In this subsection, we show how close $1+\xi$, given by eq.(3.12) and evaluated at both z_{max} and z_{min}, comes to the measured $1+\xi_{pp}$. For this comparison to be meaningful, the measured continuum should be identified with $F_0(\lambda)e^{-\tau_{GP}(\lambda)}$ of Section 3. The relatively high spectral resolution of the quasars we are considering ensures that this is usually true. Because the redshifts are not very high, there are still line-free regions which allow reasonable continuum estimation. At very high redshifts, say $z_{em} > 5$, few line-free regions exist, even with infinite spectral resolution, hence the continuum will be poorly determined. However, if the continuum is only *uniformly* underestimated or overestimated, *i.e.*, if the measured continuum is only a constant times the intrinsic one, then the measured correlation function is not affected (see Eqs. (4.1), (4.2) and (4.3)). This nice feature is in stark contrast with those encountered in measuring line equivalent width, column density and D_A, where the outcomes are very sensitive to the systematic error in continuum determination. We also note that when more data become available in the future, we will be able to overlap lots of spectra in the same narrow redshift intervals to measure the transmission correlations for each redshift. The results thus obtained can be directly compared with the theoretical calculations of Section 3.

We have chosen QSO 0837+109 to be our primary object for comparing the observed pixel-pixel transmission correlations to the theoretical predictions because of its high redshift (z_{em} = 3.326), high spectral resolution (FWHM=0.8Å) and small contamination by the identified lines (two identified lines out of a total of 87 listed lines). For this object, $z_{max} = z_{em}$ and z_{min} = 2.9892. The $1+\xi$ curves, calculated using eq.(3.12) and Model DB1 parameters and denoted by short-dashed lines, are compared with the measured $1+\xi_{pp}$ points for Q0837 (the open stars) in Fig. 5(a). We see that for small velocity separations, $\Delta v \lesssim 35$ km s^{-1}, the measured ξ_{pp} is bracketed by the two calculated curves for z_{max} and z_{min}, respectively. However, for larger Δv, the measured ξ_{pp} is significantly larger than Model DB1 predicts. A similar comparison is shown in Fig. 5(b) for the lower redshift quasar Q1247+267 (z_{em} = 2.039). We see consistency between the measured ξ_{pp} and the theoretical predictions for $\Delta v \lesssim 70$ km s^{-1}, but, again, for $\Delta v \lesssim 130$km s^{-1}, an excess in ξ_{pp} appears. We should point out that the rebinning in the data reduction process does introduce artificial correlations, but this only affects the first non-zero velocity separation bin in our measurements, and has no influence on the excess.

One possible explanation is that the excess is produced by a distribution of b in Lyα clouds, a refinement not included in the theoretical models so far, but which we examine in the following section, using Monte Carlo simulations of QSO spectra and measurement procedures exactly analogous to those used in getting ξ_{pp}. By doing lots of simulations, we can also determine the dispersions expected in ξ_{pp} measurements for a given theoretical model to give a quantitative evaluation of the significance of the excess.

Another explanation for the excess is that it signals clustering in the Lyα clouds on a scale of $\Delta v \sim 100$ km s^{-1}, a possibility we examine in detail in a following paper (Bond & Zuo 1993). We also examine the influence of ionizing field fluctuations (see also Zuo 1993b, c).

5. TRANSMISSION CORRELATIONS OF SIMULATED QSO SPECTRA

5.1 $1+\xi_{pp}$ *from Computer Simulated QSO Spectra*

We have developed a computer code to simulate the quasar spectrum (normalized by the continuum level). As in §3, we adopt the conventional joint HI column density, redshift and Doppler width distribution, $\eta(z,N,b) = A(1+z)^{\gamma_{int}} N^{-\beta} f(b)$. We assume the Doppler width distribution $f(b)$ is independent of both N and z. To give more flexibility than the simple δ-function distribution for $f(b)$ used in §3, however, we now adopt a more realistic truncated Gaussian distribution

$$f(b) = \begin{cases} \frac{\exp[-\frac{(b-b_0)^2}{2\sigma_b^2}]}{\int_{b_{min}}^{b_{max}} \exp[-\frac{(b-b_0)^2}{2\sigma_b^2}]db} & \text{if } b_{min} < b < b_{max} \\ 0 & \text{elsewhere.} \end{cases} \tag{5.1}$$

Observationally, Carswell et al (1991) have shown that $b_0 \sim 30$, $\sigma_b \sim 10$, $b_{min} \sim 12$ and $b_{max} \sim 80$, all in units of km s^{-1}. However, see Pettini et al (1990). Note that a width $b = 12$ km s^{-1} corresponds to a cloud temperature $T \simeq 10^4$K, if the broadening is dominated by random thermal motions.

To determine the normalization constant A, we force the line distribution $\eta(z,N,b)$ to produce a certain mean observed D_A value for certain z_{em} quasars (Zuo 1993a). Letting $\tau_{GP} = 0$, which is a reasonable simplification since D_A is dominated by the lines, we can calculate D_A using (Zuo 1993a)

$$1 - D_A = \frac{\int_{\lambda_1}^{\lambda_2} \exp[-\tau_{eff}(0, z_{em}, \lambda_{obs})]\, d\lambda_{obs}}{(\lambda_2 - \lambda_1)}, \tag{5.2}$$

where we have adopted $\lambda_1 = 1050(1+z_{em})\AA$ and $\lambda_2 = 1175(1+z_{em})\AA$, and τ_{eff} is calculated by

$$\tau_{eff}(0, z_{em}, \lambda_{obs}) = \frac{A}{\lambda_\alpha}\left(\frac{\lambda_{obs}}{\lambda_\alpha}\right)^{\gamma_{int}+1} \int_0^\infty f(b)db \int_{N_l}^{N_u} N^{-\beta} W_{res}(N,b)dN. \tag{5.3}$$

The mean number of clouds between z_{min} and z_{max} is given by

$$\langle n \rangle = \frac{A(1+z_{max})^{\gamma_{int}+1}}{(\beta-1)(\gamma_{int}+1)N_l^{\beta-1}} \left[1 - \left(\frac{N_l}{N_u}\right)^{\beta-1}\right] \left[1 - \left(\frac{1+z_{min}}{1+z_{max}}\right)^{\gamma_{int}+1}\right] . \tag{5.4}$$

Our simulation proceeds as follows: (1) we realize the number of lines along the line-of-sight according to a Poisson distribution with a mean $\langle n \rangle$; (2) for each line, we draw its redshift z, column density N and velocity width b from the appropriate line distribution $\eta(z,N,b)$, independently of the choices for the other lines; (3) the intrinsic spectrum, $\exp[-\tau]$ is constructed by superposing contributions to τ from each line and exponentiating; (4) we convolve the intrinsic spectrum with a Gaussian instrumental response to mimic the realistic QSO spectra of finite spectral resolution, using a discrete convolution code and discarding 'polluted points' at the two ends; (5) we measure

the simulated spectra in the same way the real quasar spectra are measured to get the transmission correlation.

To mimic the observed spectra as closely as we can, we use the same λ_{obs} sampling points as in the real QSO spectra. In the highly over-sampled simulations we report on here, we do this by selecting only those points which are closest to the real λ_{obs} sampling points, but we have checked that integration over the finite pixel size as is effectively done in real observations does not change our results. Indeed, we have found that just using only the real sampling points gives almost all the details of the over-sampled spectra, *i.e.*, the real sampling points are dense enough to reveal the fine features of the absorption lines.

Six simulated spectra for a $z_{em} = 3.326$ quasar are shown as dotted lines in Fig. 5(a), for Model DB1 parameters and for the spectral resolution of the Q0837 data. The three solid lines show the average $1 + \xi_{pp}(\Delta v)$ and its $\pm 1\sigma$ deviations, as estimated from a set of 400 simulated spectra. We see that the excess in the observed ξ_{pp} at $\Delta v \simeq 150$ km s^{-1} is indeed significant when compared with the Model DB1 predictions. In Fig. 5(b), similar curves are shown for a $z_{em} = 2.039$ quasar. Again, this shows that the excess in the observed ξ_{pp} at $\Delta v \simeq 150$km s^{-1} is significant. We also note that the simulations show large fluctuations in $1 + \xi_{pp}$ at large Δv (a regime which is not shown in Figs. 5a,b), similar to what we saw for the data in Figs. 4a,b.

To investigate the possibility that the excess in the observed ξ_{pp} at $\Delta v > 100$ km s^{-1} is produced by the dispersion in b, we have simulated absorption spectra for a truncated Gaussian $f(b)$ distribution. We have examined a number of models, labelled FB1 to FB5 and defined by the parameters listed in Table 3, which illustrate the influence of varying A, the mean b and σ_b, γ_{int} and β. These are in addition to the fixed-b models of Table 1. All FB models have $N_l = 10^{12.7}$cm^{-2} and $N_u = 10^{16.3}$cm^{-2}, and all but FB5 have $\beta = 1.7$; FB5 has $\beta = 1.57$. The A values listed in column 2 are determined, as for Table 1, by requiring a given mean value of D_A. For example, Models FB1, FB3 and FB5 are required to produce $D_A = 0.2$ for a $z_{em} = 2.875$ quasar, Zuo (1993a)'s 'Model A1' normalization; FB2 is required to give $D_A(z_{em} = 2.875) = 0.25$, Zuo (1993a)'s 'Model A7' normalization. In Zuo & Lu (1993), D_A was measured for a large sample of quasars, and γ_{int} and A were simultaneously estimated, by an extension of the method proposed by Zuo (1993a) and Lu & Zuo (1993). The parameters of Model FB4 were chosen as the values given by the 'Sample 2' QSOs in Zuo & Lu (1993), namely $\gamma_{int} = 2.87$ and $A = 7.18 \times 10^9$.

Results for Models FB1 to FB5, and also DB1, are shown in Fig. 6(a) for a $z_{em} = 3.326$ quasar. Open stars denote the measured pixel-pixel transmission correlation of Q0837+109. The curves correspond to the pixel-pixel transmission correlation functions averaged over a set of 400 simulated spectra for the following models: dotted, DB1; short-dashed, FB1; long-dashed, FB2; solid, FB3; dot-short-dashed, FB4. In addition, the $\pm 1\sigma$ lines for Model FB3 (with the largest b-variation) are also shown by solid lines. In Fig. 6(b), similar results are presented for Q1247+267 ($z_{em} = 2.039$).

Fig. 6(a) shows that $1 + \xi_{pp}$ for Models FB1 and DB1 are quite similar, except FB1 has a little more correlation at $\Delta v \simeq 100$ km s^{-1}. Model FB2, with a higher normalization, produces more absorption, *i.e.*, a larger D_A, and this is reflected in its larger correlation, which actually is larger than the observed ξ_{pp} of QSO 0837+109 at velocity separations $\Delta v < 50$ km s^{-1}; however, it is still significantly smaller than the observed one at separations $\Delta v \simeq 150$ km s^{-1}. This demonstrates that, although the uncertainty in D_A and hence the normalization could easily shift the simulated ξ_{pp} to match the observed one at separations $\Delta v < 70$km s^{-1}, since FB1 and FB2 produce very similar ξ_{pp} at $\Delta v \simeq 150$ km s^{-1} it cannot explain the excess. Adding clustering of absorption lines

at velocity separation scales a few times the typical line widths will boost transmission correlations at both very small scales and at $\Delta v \simeq 150$ km s^{-1}, hence it is possible that the FB1 or FB2 parameters can work, with this extra ingredient. Model FB3, with $b_0 = 40$ km s^{-1} and $\sigma_b = 25$ km s^{-1}, does produce significant transmission correlations at $\Delta v \sim 100$km s^{-1}, and within the 1-σ error limits, this model matches (barely) the real measurement of QSO 0837 at separations $\Delta v > 150$ km s^{-1}. Model FB4 leads to a ξ_{pp} which is significantly smaller than the observed ξ_{pp} of Q0837 at all separation scales $\Delta v < 250$ km s^{-1}. Because there are relatively more strong lines in our Model FB5, which has a $\beta = 1.57$, the resulting ξ_{pp} is larger than that of Model FB1, but is still significantly smaller than the measured values at $\Delta v \simeq 150$ km s^{-1}.

Fig. 6(b) shows that Models DB1, FB1 and FB4 match the observed ξ_{pp} of QSO 1247+267 reasonably well at $\Delta v < 100$km s^{-1}, but are all significantly smaller than the observed one at $\Delta v \simeq 150$ km s^{-1}. Models FB2 and FB5 produce too much correlation at small separation scales and still fall short of the observed one at $\Delta v \simeq 150$ km s^{-1}. This time our excess velocity width model, FB3, does match the observed ξ_{pp} quite well at $\Delta v > 100$ km s^{-1}, and is consistent at smaller separations.

5.2 Insensitivity of the Transmission Correlation to Observational Noise

We now discuss the effect that noise in the observed QSO spectra has on the transmission correlation function. We consider here mainly two sources of noise, the photon noise in the QSO flux (including absorption by intervening absorbers), and the sky background subtraction noise. We develop a procedure to simulate such noise below. Other noise sources can easily be added, following this procedure.

Consider the ith wavelength pixel in a quasar spectrum (real or simulated). Denote the quantum efficiency of the pixel by q_i. If $q_i = 1$, then the photon count in this ith wavelength bin is

$$n_i = (n_{spect} + n_{sky}) - n'_{sky}, \tag{5.5}$$

where n_{spect} is the photon number contributed by the quasar flux, which includes absorption by intervening absorbers, n_{sky} is the sky contribution which comes from the same sky area covered by the quasar image, and n'_{sky} is the average over some blank sky areas. We have omited the subscript "i" for the right-hand-side variables in eq.(5.5) to achieve clarity. We shall do the same below whenever we judge it will not generate confusion.

Usually n_{spect} dominates over n_{sky}, since, to achieve high spectral resolution, only the most luminous quasars are observed; however, in the line center regions n_{sky} may dominate, since n_{spect} may be nearly zero there. For the variance $\sigma(n_i)$ in the ith bin, we have

$$\sigma^2(n_i) = q_i\,\overline{n}_{spect} + q_i\,\overline{n}_{sky}\ . \tag{5.6}$$

Here, and in the following, we assume that $\sigma(n'_{sky}) = 0$. This is a good assumption if n'_{sky} is obtained by averaging over a much larger blank sky area than the size of the quasar image. If this is not true, then eq.(5.6) can be easily modified. The pixel signal-to-noise ratio S/N is then given by

$$\frac{\mathrm{S}}{\mathrm{N}} = \frac{\sqrt{q_i}\,\overline{n}_{spect}}{\sqrt{\overline{n}_{spect} + \overline{n}_{sky}}} \approx \begin{cases} \sqrt{q_i\,\overline{n}_{con}} & \text{line free region} \\ \dfrac{\sqrt{q_i}\,\overline{n}_{spect}}{\sqrt{\overline{n}_{sky}}} & \text{line center region,} \end{cases} \tag{5.7}$$

where n_{con} is the photon number contributed by the quasar continuum, which includes the Gunn-Peterson absorption.

We do our simulations according to the following formula:

$$e^{-\tau}|_{simul} = \frac{(q_i\,\overline{n}_{spect})|_{simul}}{q_i\,\overline{n}_{con}} + \frac{(q_i\,\overline{n}_{sky})|_{simul} - q_i\,\overline{n}_{sky}}{q_i\,\overline{n}_{con}}\,, \tag{5.8}$$

where the subscript "simul" means choose a Poisson deviate from a Poisson distribution whose mean value is given in the parenthesis. Here the mean value $q_i\,\overline{n}_{spect}$ is the simulated transmission (after convolution with an instrumental response profile) multiplied by $q_i\,\overline{n}_{con}$. The noise is added only after the convolution with the response function, and is taken to be Poissonian. In the Appendix, we give a detailed proof that noise in different wavelength bins is not correlated, even after going through a spectrograph with finite instrumental resolution.

To complete our prescription for the simulation, we need to know $q_i\,\overline{n}_{con}$ and $q_i\,\overline{n}_{sky}$. Letting the quasar continuum level (including the Gunn-Peterson absorption) be described by f_ν, we have $\overline{n}_{con} \propto f_\nu d\ln\nu$, where $d\ln\nu$ is the size of the ith bin. In our case here, $d\ln\nu$ is the same for all wavelength bins (with a few exceptions). Since the observed relative intensity in the line free region is proportional to $q_i f_\nu$, we know that $q_i\,\overline{n}_{con}$ is proportional to the observed relative intensity or counts in the line-free region. Since the noise is source dominated for the data considered here, in a line-free region we have $(\mathrm{S/N})^2 = q_i\,\overline{n}_{con}$. To simulate a realistic quasar spectrum, we first check the observed spectrum, identify a wavelength pixel in a line-free region and estimate the pixel signal-to-noise ratio. We then square S/N to get $q_i\,\overline{n}_{con}$ for this wavelength bin. Denoting the fitted continuum level to the observed relative intensity at the ith bin by f_i, then, for an arbitrary jth wavelength bin, we have $q_j\,\overline{n}_{con} = (f_j/f_i)q_i\,\overline{n}_{con}$. For the sky background noise, we assume that $\overline{n}_{sky}$ is a constant which does not depend on wavelength. This is a reasonable assumption since the spectral coverage for the cases considered in this paper is relatively narrow. We take $\overline{n}_{sky}$ to be a free parameter and try various $\overline{n}_{con}/\overline{n}_{sky}$ values in our simulations.

For Q0837+109, we chose to normalize to the wavelength bin at $\lambda_{obs} = 4950$Å which has a continuum level $f_i = 27.27$. S/N is about 10 there, so we adopt a $q_i\,\overline{n}_{con} = 100$ for this normalization bin. We also chose to use $q_i\,\overline{n}_{sky} = 10$. For simplicity, in the following discussion we assume q_i is independent of wavelength. This is reasonable as long as the wavelengths are not close to the blue end of the observed spectrum. Compare the observed Q0837 spectrum from Sargent, Boksenberg & Steidel (1988), Fig. 7(a), with simulations for Models FB1 (Fig. 7b) and FB3 (Fig. 7c). We see that our simulations mimic the observed spectrum quite well. Near the emission redshift, where the flux level is boosted significantly by the Lyα emission wing, S/N is very large. For Q1247+267, we chose to normalize at the wavelength bin $\lambda_{obs} = 3330$Å with $f_i = 267.39$. S/N there is about 20, so we adopt $q_i\,\overline{n}_{con} = 400$ at this bin. We set $q_i\,\overline{n}_{con} = 40$. The Sargent et. al. data is shown in Fig. 8(a), and simulated spectra for FB1 and FB3 parameters are shown in (b) and (c), respectively. These figures show that, at a visual level, Model FB3 mimics the real spectra more closely than Model FB1, especially in the low z_{em} (Q1247) case. Of course, this is just one realization for each model, but the quantitative comparison using the transmission correlation function supports this. However, it is possible that a little clustering in Model FB1 at velocity separation scales a few times the typical line widths may mimic the real spectra much better.

We have measured some simulated noisy spectra to examine the influence that the noise has on the measured pixel-pixel transmission correlation function. Some results are shown in Fig. 9. Each curve represents the average of a set of 400 simulated spectra, all made using Model FB1

parameters. The solid line is the noise-free case. The other cases have varying amounts of noise: the dotted line is for $q_i\,\overline{n}_{con} = 100$ and $q_i\,\overline{n}_{sky} = 10$; the short-dashed line is for $q_i\,\overline{n}_{con} = 25$ and $q_i\,\overline{n}_{sky} = 2.5$; and the long-dashed line is for $q_i\,\overline{n}_{con} = 100$ and $q_i\,\overline{n}_{sky} = 100$. The open stars denote the measured $1 + \xi_{pp}$ for Q0837. In Fig. 10, we show $\sigma(1 + \xi_{pp})$ as a function of Δv for a $z_{em} = 3.326$ quasar. All the curves are derived from the same sets of simulations done for Fig. 9. These two figures show that the noise effect is not important at all, even for very low S/N spectra, and the noisy ξ_{pp} is very close to that of the noise-free simulations, except in the zeroth bin ($\Delta v = 0$). This is, of course, expected since the noise is Poissonian, that is, is correlated with itself (therefore affecting the zero separation bin), but not with the noise in different wavelength bins.

It seems that we don't need very high S/N spectra to get very good ξ_{pp} measurements. This is true especially *if* the continuum determination is not seriously affected by the high noise level. We point out that the existing high resolution echelle spectra are ideal for the pixel-pixel transmission correlation analysis advocated here, since they can be used to probe even smaller velocity separations, and the correlation signal will be boosted by high spectral resolution at small velocity separation scales.

6. DISCUSSION

6.1 Comparing The Measured D_A with Model Predictions

Our models are normalized to produce D_A values which are acceptable within the uncertainties of observations. In this subsection, we check this by comparing the predicted D_A values from our various models with the measure D_A values for Q0837 and Q1247. For the purposes of D_A determination, we do not remove the identified lines in the wavelength interval we are considering. For Q0837, the measured $D_A = 0.281$ for λ_{obs} from 4849.55Å to 5258.99Å. For this same λ_{obs} interval, Models DB1, FB1 and FB3 predict $D_A = 0.332$; FB2 gives a large $D_A = 0.406$; and Model FB4 leads to $D_A = 0.269$. For Q1247, the measured $D_A = 0.071$ for λ_{obs} from 3250.16Å to 3694.42Å. For the same λ_{obs} interval, Models DB1, FB1 and FB3 predict $D_A = 0.094$; FB2 gives a large $D_A = 0.120$; and FB4 leads to $D_A = 0.071$, the same as the measured value. The theoretically predicted dispersion in D_A is very small (Zuo 1993a, Lu & Zuo 1993, Zuo & Lu 1993), since a large number of lines are involved in its determination. Thus the large dispersion in the measured D_A values indicates that measurement errors must play a major role. However, for the Q1247 spectrum, which has low redshift and very high S/N, the measured D_A should be quite accurate. This suggests that Model FB2's normalization leads to an overestimate of the absorption produced by Lyα forest lines. Even so, FB2 still cannot account for the large ξ_{pp} observed at $\Delta v \simeq 150$ km s^{-1}.

6.2 Results for Some Other Quasars

We have studied in some detail the spectra of Q0837 and Q1247, and have found a significant excess in the observed ξ_{pp} at $\Delta v \simeq 150$ km s^{-1}. What about the other quasars in our sample? In Fig. 11 we compare simulated results with the measured $1 + \xi_{pp}$ for 4 other QSOs, (a) 0424-131, (b) 2206-199, (c) 1511+091 and (d) 0014+813. In each panel, the open stars are the measurements from the real quasar spectrum. The 3 dashed lines are the mean $1 + \xi_{pp}$ and its 1-σ limits from a set of 400 simulations using Model FB1 parameters, while the 3 solid lines are for Model FB3 parameters. Notice that the Q0424 spectrum has a FWHM=0.8Å, while the FWHM=1.5Å for the other 3 QSO spectra. As can be seen from Figs. 4(a) and 11(a), the measured ξ_{pp} for Q0424

is exceptionally large and our 2 model calculations are well below it. The measured D_A between $\lambda_{obs} = 3500\AA$ and $3848.81\AA$, including the identified lines, is 0.162, which is significantly larger than Models FB1 and FB3 predict, $D_A = 0.115$. If we remove the identified lines, the measured $D_A = 0.142$, still larger than Models FB1 and FB3 can account for, but it is comparable to the prediction for Model FB2, $D_A = 0.146$. Renormalizing to a larger D_A value, such as Model FB2 has, can match the observed ξ_{pp} at small velocity separation scales, but it is clear that even Model FB2 will not explain the observed ξ_{pp} excess at $\Delta v \simeq 150$ km s^{-1}. For the 3 FWHM=1.5$\AA$ QSO spectra, we also see that the observed ξ_{pp} values decrease more slowly then the simulated ones do. Again the bottom line is that Model FB1 type models, with $b_0 \simeq 30$ km s^{-1} and $\sigma_b \simeq 10$ km s^{-1}, cannot explain the observed large ξ_{pp} at $\Delta v \simeq 150$ km s^{-1}, while Model FB3 type models, with larger b_0 and σ_b, are barely consistent with the observations.

6.3 What About The Proximity Effect?

Near the quasar emission redshift along the line-of-sight, the ionizing field is significantly enhanced by radiation from the quasar itself, and Lyα clouds there are more ionized than average. This may explain the observed "proximity" or "inverse" effect, which suggests there is a systematic deficit of Lyα absorption lines near the quasar emission redshift. We now examine how this enhanced ionizing field near the quasar affects our ξ_{pp} results.

We assume that the mean intensity of the ionizing background at the Lyman limit frequency ν_L is $J_{\nu_L} = 10^{-21} J_{-21}$ergs s^{-1}cm^{-2}Hz^{-1}sr^{-1}, that its spectrum is flat from ν_L to $4\nu_L$, beyond which the flux level drops significantly due to HeII Lyman continuum absorption by Lyα clouds (see Zuo & Phinney 1993). It really does not matter what the precise spectral shape is at $\nu > 4\nu_L$ since the HI absorption cross section is negligibly small at high frequencies. For the quasar at the end of the line of sight, we assume its monochromatic luminosity is given by $L_\nu = 10^{31} L_{31} (\nu/\nu_L)^{-1.5}$ergs s^{-1}Hz^{-1}. For an Einstein-de Sitter universe ($q_0 = 1/2$), it is straightforward to show that the neutral hydrogen column density N of an absorption line of redshift z near z_{em} is reduced to

$$N' = \frac{N}{1+\omega}\,, \tag{6.1}$$

where

$$\omega = 1.253 \times 10^{-7} \left(\frac{L_{31} h^2}{J_{-21}}\right) (1+z)^3 \left(\frac{1+z}{1+z_{em}}\right)^{2.5} \left(1 - \sqrt{\frac{1+z}{1+z_{em}}}\right)^{-2} . \tag{6.2}$$

We have performed simulations for a $z_{em} = 3.326$ quasar that use eq.(6.1) to reduce N near z_{em}. Our simulated spectra for three different $L_{31}h^2/J_{-21}$ values are shown in Fig. 12. In this figure the first panel is the spectrum without the "proximity effect", which is the same realization as the Fig. 12(b) spectrum but without noise added. The second panel of Fig. 12 is the simulated spectrum for $L_{31}h^2/J_{-21} = 1$, the third panel for $L_{31}h^2/J_{-21} = 10$ and the fourth one for $L_{31}h^2/J_{-21} = 100$. All 4 panels are for the same realization of the line positions and properties. It can be seen that the proximity effect is significant if $L_{31}h^2/J_{-21} > 10$. Comparison with the real spectrum of Q0837 in Fig. 6(a) suggests that we can rule out values of $L_{31}h^2/J_{-21}$ in excess of 10.

In Fig. 13 we show how ξ_{pp} is affected by the proximity effect. The open stars are the results from the real spectrum of Q0837, the 3 solid lines are the mean $1+\xi_{pp}$ and its 1-σ limits from a set of 400 simulations using Model FB1 parameters and $L_{31}h^2/J_{-21} = 0$, i.e., no proximity effect, the 3 long dashed lines are for $L_{31}h^2/J_{-21} = 1$, the three dotted lines are for $L_{31}h^2/J_{-21} = 10$ and the 3

short dashed lines are for $L_{31}h^2/J_{-21} = 100$. In all of these simulations, no noise was added. Again we see that if $L_{31}h^2/J_{-21} > 10$ then the resulting ξ_{pp} is significantly reduced at small velocity separation scales. However, it is also clear that proximity cannot explain the observed excess in ξ_{pp} at $\Delta v = 150$ km s^{-1}: the correction there is very small.

For Q0837+109, Lu et al. (1991) estimated the continuum flux at the observed Lyman limit frequency to be 1.2×10^{-27}ergs s^{-1} cm^{-2}Hz^{-1}. This leads to $L_{31} = 0.6h^{-2}$ for the $z_{em} = 3.326$ quasar. According to Zuo & Phinney (1993), $J_{-21} \simeq 0.4$ at the redshift we are interested in, from quasar contributions alone. Combining the two implies that $L_{31}h^2/J_{-21}$ cannot be much larger than 1.5 for Q0837. Figures 12 and 13 then show that the proximity effect is not very important, although it is certainly not negligible. With a large sample of good quality QSO spectra, we may be able to use ξ_{pp} to explore the proximity effect and to determine the mean intensity of the ionizing background, J_{-21}.

6.4 Advantages of ξ_{pp} over Line Counting for Distribution Estimation

One would like to think that the $f(b)$ distribution and the neutral hydrogen column density distribution of QSO Lyα forest lines can be well-determined by the line counting method using very high spectral resolution and very high S/N spectra. But up to now this has not been the case. The high spectral resolution data used for b and N distributions have lacked the exceptionally high S/N one would like to have. Also the measured N value is very sensitive to the adopted continuum level, and the measured b value may be as well. At very high redshift, the lines are badly blended and there are few line-free regions that one can use to obtain a sensible continuum, even with infinite spectral resolution. Furthermore, when several lines are blended together, it is no easy task to separate them properly to get the right b and N for each component. These complications are very well appreciated by people working in this field and they are usually the source of controversies, especially when the noise effect is mixed in (see *e.g.*, Rauch et al. 1993). Our method sidesteps most of these difficulties. At the very least, it is a good complementary method, and deserves further exploration.

7. CONCLUSIONS

We summarize our principal results:

1. We have developed a technique for calculating the transmission correlation produced by randomly distributed lines, which we applied to various Lyα forest line distribution models that illustrate the broad features expected in observed transmission correlations.

2. We have introduced an operationally straightforward procedure to measure the pixel-pixel transmission correlation function for observed quasar spectra. We have applied this method to 12 Sargent, Boksenberg & Steidel QSO spectra which are of high quality both in spectral resolution and S/N.

3. The observational transmission correlations were compared with both theoretical predictions and the correlations measured from simulated quasar spectra. These simulations of a given quasar's spectrum use the same wavelength sampling points, instrumental resolution, continuum information and noise properties as for the real spectrum so that we mimic the observed spectrum as closely as we can.

4. Comparison of the transmission correlations obtained from simulated spectra with the observed $1 + \xi_{pp}$ has led to the discovery that there is a significant excess in the observed pixel-pixel transmission correlation function ξ_{pp} at $\Delta v \simeq 150$ km s^{-1}, if the Carswell et al. (1991) $f(b)$ distribution — a Gaussian with a mean $b_0 = 30$ km s^{-1} and $\sigma_b = 10$ km s^{-1} — is used in the simulations. One explanation is that the Lyα forest lines are actually clustered at velocity separation scales $\Delta v \simeq 150$ km s^{-1}. Another explanation is that $f(b)$ should have more large b clouds and a larger dispersion in b than the Carswell et al. distribution gives. The observed results are roughly consistent with models having $b_0 = 40$ km s^{-1} and $\sigma_b = 25$ km s^{-1}.

5. We have used simulated spectra that add experimental noise to show that ξ_{pp} is not sensitive to noise at all except in the zeroth bin ($\Delta v = 0$). This is because noise in different wavelength bins is not correlated, as we demonstrated in the Appendix. An important property of the measured ξ_{pp} is that it is not affected if the continuum is underestimated or overestimated *uniformly* by a constant factor. More generally, we believe that the measured ξ_{pp} should be quite robust to errors in the continuum determination, since we are probing at velocity separation scales which are less than several typical line widths. These nice features should be contrasted with those of traditional line counting methods, where the outcome is very vulnerable to the noise level and the errors in continuum estimation. Thus, with the burst of high quality data promised by the upcoming 10-meter class telescopes in the near future, we believe that the transmission correlation method introduced here will furnish a powerful tool for extracting information from the crowded Lyα forest.

We would like to thank Wal Sargent for allowing us to use the Sargent, Boksenberg & Steidel QSO spectra in digital form. We would also like to thank Limin Lu for providing his continuum fits. Conversations with Simon Lilly, Tom Loredo, Don Schneider and Howard Yee have been helpful in our understanding of noise in quasar spectra. This work was supported by the NSERC of Canada. JRB was supported by a Canadian Institute for Advanced Research Fellowship.

APPENDIX: Noise in Resolution-Degraded Spectra

In this Appendix, we give a mathematical demonstration that the original uncorrelated photon noise at two different wavelength bins remains uncorrelated after going through a spectrograph with a finite spectral resolution. The critical feature is that the transition of a given photon from an initial wavelength bin to a final wavelength bin is described by a probability function, and not by a convolution of the flux. The latter would have led to correlation if the separation between two final state wavelength bins was less than the width of the instrumental response profile.

Suppose that we integrate for some time and group photons arriving in front of a telescope into the wavelength bins $i = 0, \pm 1, \pm 2, ..., \pm\infty$. In each bin, the photon number obeys Poisson statistics with a mean $\overline{n}_i$. Here we only consider a set of fixed $\overline{n}_i$. After passing through the telescope and the spectrograph, these photons end up in detector wavelength bins $\alpha = 0, \pm 1, \pm 2, ..., \pm\infty$. We do not assume that the two sets of wavelength bins are the same. Let us assume that our instrumental point spread function or response function, $q_{i\alpha_K}$, has a finite width. $q_{i\alpha_K}$ is the probability that a photon in initial bin i ends up in a final state bin α_K.

Consider a realization of the original photon counts n_i, drawn from a Poisson distribution with fixed mean $\overline{n}_i$ for each bin i. Thus n_i and n_j are uncorrelated for $i \neq j$. If we were to convolve the generated randoms digits with the instrumental response function $q_{i\alpha_K}$, photon numbers in the detector wavelength bins α_K would be correlated over separations below the width of $q_{i\alpha_K}$, since a photon in an initial state wavelength bin in front of the telescope would contribute partly to different α_K. However, photons do not break up. The instrumental convolution of the photon flux is really a probabilistic thing; that is, the response function $q_{i\alpha_K}$ should be viewed as a transition probability describing the likelihood that an incoming photon in front of the telescope will be channeled into detector bin α_K. It is then a straightforward exercise in probability theory to demonstrate that the photon numbers in different α_K detector bins are uncorrelated, no matter how close the wavelength bins. We now prove this statement.

Consider a wavelength bin i in front of the telescope. Let $p_{i\alpha_K}(m_{i\alpha_K}|\overline{n}_i)$ be the probability that the α_K bin detects $m_{i\alpha_K}$ photons from the ith bin. It is a Poisson-distribution with mean $q_{i\alpha_K}\overline{n}_i$:

$$p_{i\alpha_K}(m_{i\alpha_K}|\overline{n}_i) = \frac{q_{i\alpha_K}^{m_{i\alpha_K}}\overline{n}_i^{m_{i\alpha_K}}}{m_{i\alpha_K}!}e^{-q_{i\alpha_K}\overline{n}_i} \ . \qquad (A.1)$$

We now show that the joint probability for the $\{m_{i\alpha_K}\}$ is just the product of these individual Poissonians, which demonstrates that the final state bin counts are statistically independent of each other. Suppose the initial state bin i has n_i photons. It is drawn from a Poissonian with mean $\overline{n}_i$,

$$p_i(n_i|\overline{n}_i) = \frac{\overline{n}_i^{n_i}}{n_i!}e^{-\overline{n}_i} \ . \qquad (A.2)$$

The way these i-bin photons are redistributed into the α_K bins is described by the standard multinomial distribution:

$$P(m_{i\alpha_1}, m_{i\alpha_2}, m_{i\alpha_3}, ...|n_i) = n_i! \prod_K \frac{q_{i\alpha_K}^{m_{i\alpha_K}}}{m_{i\alpha_K}!} \ , \quad \text{where} \sum_K m_{i\alpha_K} = n_i \ . \qquad (A.3)$$

(The problem is akin to distributing balls into boxes, labelled α_K, with some boxes being more likely to get a ball than others, with weight $q_{i\alpha_K}$.) We want to average over all possible n_i to get this joint probability given just the mean $\overline{n}_i$:

$$\begin{aligned} P(m_{i\alpha_1}, m_{i\alpha_2}, m_{i\alpha_3}, ...|\overline{n}_i) &= \sum_{n_i} P(m_{i\alpha_1}, m_{i\alpha_2}, m_{i\alpha_3}, ...|n_i) P(n_i|\overline{n}_i) \\ &= \prod_K \frac{q_{i\alpha_K}^{m_{i\alpha_K}}}{m_{i\alpha_K}!} \prod_K \overline{n}_i^{m_{i\alpha_K}} e^{-q_{i\alpha_K}\overline{n}_i} \\ &= \prod_K p_{i\alpha_K}(m_{i\alpha_K}|\overline{n}_i) \ . \end{aligned} \tag{A.4}$$

In the second step we have used the normalization $\sum_K q_{i\alpha_K} = 1$ and also replaced n_i by $\sum_K m_{i\alpha_K}$. This result also explicitly demonstrates that the mean photon number in bin α_K that began in bin i is indeed $\overline{m}_{i\alpha_K} = q_{i\alpha_K}\overline{n}_i$.

Since the initial state counts are independent of each other, the redistribution into final state counts is also independent. Thus to get the joint probability distribution for the total counts in bin α_K,

$$M_{\alpha_K} = \sum_i m_{i\alpha_K} \ , \tag{A.5}$$

we just take the product of terms (A.4), one for each i, and sum over the $\{m_{i\alpha_K}\}$ configurations which add up to M_{α_K}:

$$\begin{aligned} P(M_{\alpha_1}, M_{\alpha_2}, M_{\alpha_3}, ...|\overline{n}_1, \overline{n}_2, \overline{n}_3, ...) &= \sum_{\{m_{i\alpha_K}\}\ configs} \prod_K \prod_i \frac{(q_{i\alpha_K}\overline{n}_i)^{m_{i\alpha_K}}}{m_{i\alpha_K}!} e^{-q_{i\alpha_K}\overline{n}_i} \\ &= \prod_K \exp[-\sum_i q_{i\alpha_K}\overline{n}_i] \frac{1}{M_{\alpha_K}!} \left\{ \sum_{\{m_{i\alpha_K}\}\ configs} M_{\alpha_K}! \prod_i \frac{(q_{i\alpha_K}\overline{n}_i)^{m_{i\alpha_K}}}{m_{i\alpha_K}!} \right\} . \end{aligned}$$

We have inserted an $M_{\alpha_K}!$ to make the term in big curly brackets immediately recognizable as the multinomial distribution. It is summed over all possible configurations which add up to M_{α_K}, and, of course, this is just

$$\Big(\sum_i q_{i\alpha_K}\overline{n}_i\Big)^{M_{\alpha_K}} \ .$$

We therefore finally have

$$P(M_{\alpha_1}, M_{\alpha_2}, M_{\alpha_3}, ...|\overline{n}_1, \overline{n}_2, \overline{n}_3, ...) = \prod_K \frac{\overline{M}_{\alpha_K}^{M_{\alpha_K}}}{M_{\alpha_K}!} \exp[-\overline{M}_{\alpha_K}] \ , \quad \text{where } \overline{M}_{\alpha_K} \equiv \sum_i q_{i\alpha_K}\overline{n}_i \ , \tag{A.6}$$

a product of independent Poissonian distributions, with the mean number in bin α_K given by the convolution of the mean number in the initial state with a response function $q_{i\alpha_K}$.

So far in this Appendix, we have dealt with photon counting statistics for a given set of $\overline{n}_i$. For a given theoretical model, say one characterized by the parameters $\gamma_{int}, \beta, b_0, \sigma_b, ...$, different realizations of the line distribution result in different $\overline{n}_i$, which will be correlated, because of the finite width of the absorption lines and possibly because of clustering. The joint probability distribution for the $\overline{n}_i$, $P(\overline{n}_1, \overline{n}_2, \overline{n}_3, ...|\gamma_{int}, \beta, ...)$, therefore does not split into independent products.

The way the correlations that we measure in the M_{α_K} enter is through this joint probability for $\{\overline{n}_i\}$ configurations:

$$P(M_{\alpha_1}, M_{\alpha_2}, M_{\alpha_3}, ...|\gamma_{int}, \beta, ...) = \sum_{\{\overline{n}_i \ configs\}} P(M_{\alpha_1}, M_{\alpha_2}, M_{\alpha_3}, ...|\overline{n}_1, \overline{n}_2, \overline{n}_3, ...) \times P(\overline{n}_1, \overline{n}_2, \overline{n}_3, ...|\gamma_{int}, \beta, ...) \ . \qquad (A.7)$$

It is this correlation that the transmission correlation function measures, and there is no extra correlation arising from photon counting statistics.

TABLE 1
Model Parameters for $1 + \xi_0(\Delta v)$ Calculations

Model	β	A	γ_{int} (km s^{-1})	b	N_l (cm^{-2})	N_u (cm^{-2})
DB1	1.7	1.1×10^{10}	2.75	30	$10^{12.7}$	$10^{16.3}$
DB2	1.7	1.1×10^{10}	2.75	30	$10^{12.0}$	$10^{16.3}$
DB3	1.7	1.1×10^{10}	2.75	30	$10^{12.7}$	$10^{17.0}$
DB4	1.7	1.9×10^{10}	2.3	30	$10^{12.7}$	$10^{16.3}$
DB5	1.7	2.8×10^{10}	2.0	30	$10^{12.7}$	$10^{16.3}$
DB6	1.57	1.7×10^{8}	2.75	30	$10^{12.7}$	$10^{16.3}$
DB7	1.7	1.3×10^{10}	2.75	20	$10^{12.7}$	$10^{16.3}$

TABLE 2
QSO Sample Used in Transmission Correlation Measurements

Object	z_{em}	FWHM ($\AA$)	λ_{obs} Range ($\AA$)	ID Line/Total Line
Q1159+124	3.502	0.8, 1.5	4617.79—5472.95	12/110
Q0014+813	3.377	1.5	4761.31—5320.99	13/86
Q0837+109	3.326	0.8	4849.55—5258.99	2/87
Q0114–089	3.199	1.5	4760.00—5104.60	0/50
Q1511+091	2.878	1.5	4201.15—4560.53	3/51
Q0142–100	2.727	0.8	3822.86—4530.80	10/125
Q2206–199	2.559	1.5	3820.00—4326.57	8/46
Q1623+269	2.526	0.8, 1.1	3616.69—4286.45	28/83
Q0237–233	2.222	0.8	3345.10—3916.89	26/87
Q0424–131	2.166	0.8	3500.00—3848.81	7/50
Q1247+267	2.039	0.8	3250.16—3694.42	4/48
Q1017+280	1.928	0.8	3200.00—3559.48	5/34

TABLE 3
Model Parameters for $1 + \xi_{pp}(\Delta v)$ Simulations

Model	A	γ_{int}	β	b_0 (km s^{-1})	σ_b (km s^{-1})	b_{min} (km s^{-1})	b_{max} (km s^{-1})
FB1	1.10×10^{10}	2.75	1.7	30	10	12	80
FB2	1.42×10^{10}	2.75	1.7	30	10	12	80
FB3	9.55×10^{9}	2.75	1.7	40	25	10	100
FB4	7.18×10^{9}	2.87	1.7	30	10	12	80
FB5	1.70×10^{8}	2.75	1.57	30	10	12	80

REFERENCES

Bechtold, J., Green, R. F., Weymann, R. J., Schmidt, M., Estabrook, F. B., Sherman, R. D., Wahlquist, H. D., & Heckman, T. M., 1984, ApJ 281, 76

Bond, J. R., & Zuo, L. 1993. ApJ, in preparation

Carswell, R. F., Whelan, J. A. J., Smith, M. G., Boksenberg, A., & Tytler, D., 1982, MNRAS 198, 91

Carswell, R. F., Lanzetta, K. M., Parnell, H. C., & Webb, J. K. 1991. ApJ, 371, 36

Giallongo, E., & Cristiani, S., 1990, MNRAS 247, 696

Hunstead, R. W., Murdoch, H. S., Peterson, B. A., Blades, Jauncey, D. L., Wright, A. E., Pettini, M., & Savage, A., 1986, ApJ 305, 496

Jenkins, E. B., & Ostriker, J. P., 1991, ApJ 376, 33

Liu, X. D., & Jones, B. J. T., 1988, MNRAS 230, 481

Lu, L., Wolfe, A. M., & Turnshek, D. A. 1991, ApJ 367, 19

Lu, L., & Zuo, L. 1993. ApJ, submitted

Lynds, C. R. 1971. ApJ, 164, L73

O'Brien, P. T., Gondhalekar, P. M., & Wilson, R., 1988, MNRAS 233, 801

Oke, J. B., & Korycansky, D. G., 1982, ApJ 255, 11

Parnell, H. C., & Carswell, R. F., 1988, MNRAS 230, 491

Pettini, M., Hunstead, R. W., Smith, L. J., & Mar, D. P. 1990. MNRAS, 246, 545

Press, W. H., Rybicki, G. B., & Schneider, D. P. 1993. preprint

Press, W. H., & Rybicki, G. B. 1993. preprint

Rauch, M., Carswell, R. F., Webb, J. K. & Weymann, R. J., 1993, MNRAS, 260, 589

Sargent, W. L. W., Young, P. J., Boksenberg, A., & Tytler, D. 1980. ApJS, 42, 41

Sargent, W. L. W., Boksenberg, A., & Steidel, C. C. 1988. ApJS, 68, 539

Schneider, D. P., Schmidt, M., & Gunn, J. E., 1989a, AJ 98, 1507

Schneider, D. P., Schmidt, M., & Gunn, J. E., 1989b, AJ 98, 1951

Schneider, D. P., Schmidt, M., & Gunn, J. E., 1991, AJ 102, 837

Spitzer, L. Jr. 1978. *Physical Processes in the Interstellar Medium*, 53

Steidel, C. C., & Sargent, W. L. W., 1987, ApJ 313, 171

Trevese, D., Giallongo, E., & Camurani, L., 1992, ApJ 398, 491

Webb, J. K. 1987, private communication via Dr. W. L. W. Sargent

Webb, J. K., Barcons, X., Carswell, R. F., & Parnell, H. C., 1992, MNRAS 255, 319

Young, P. J., Sargent, W. L. W., Boksenberg, A., Carswell, R. F., & Whelan, J. A. J., 1979, ApJ 229, 891

Zuo, L. 1993a. A&A, in press

Zuo, L. 1993b. MNRAS, 258, 36

Zuo, L. 1993c. MNRAS, 258, 45

Zuo, L., & Lu, L. 1993. ApJ, submitted

Zuo, L., & Phinney, E. S. 1993. ApJ, in press

FIGURE CAPTIONS

Fig. 1. The transmission correlation function $1 + \xi(\Delta v)$ as a function of $y \equiv |\Delta v|/\delta v$ for our toy model of identical uncorrelated clouds, each having depth τ_0 and width δv that together result in an average depth $\langle \tau(v) \rangle \equiv N_l \tau_0$. The models shown are: (a) $\tau_0 = 0.5,\ N_l = 0.5$; (b) $\tau_0 = 2,\ N_l = 0.5$; and (c) $\tau_0 = 0.5, N_l = 2$. The effect of finite instrumental resolution is shown by the sequence of curves labelled by various $y_{\mathcal{I}} \equiv v_{\mathcal{I}}/\delta v$.

Fig. 2. The transmission correlation function, $1+\xi_0(\Delta v)$, produced by uncorrelated Lyα forest lines drawn from a power law distribution in HI column depth and redshift, is plotted as a function of $\Delta v/b$ for the redshifts shown. The models shown, with parameters defined in Table 1, are (a) DB1, DB2 and DB3, (b) DB4 and DB5, and (c) DB6 and DB7. The curves are for infinite instrumental resolution. The effect of decreasing resolution, parameterized by the Gaussian width σ_λ, is shown in (d) for the model DB1 calculated at $z = 4.5$.

Fig. 3. The spectrum of Q0837+109 from Sargent, Boksenberg & Steidel (1988) and the continuum fit (the dashed line).

Fig. 4. (a) The measured pixel-pixel transmission correlation $1 + \xi_{pp}(\Delta v)$ as a function of Δv for six quasars of spectral resolution FWHM= $0.8\mathring{A}$; (b) the same, but for six quasars of resolution FWHM$\sim 1.5\mathring{A}$.

Fig. 5. (a) The two short-dashed lines are $1+\xi(\Delta v)$ curves for Model DB1 with a FWHM= $0.8\mathring{A}$ for $z = 3.326$ and $z = 2.989$. The open stars denote the measured pixel-pixel transmission correlation of Q0837+109. The six dotted lines are the results measured from six simulated spectra, calculated by the same procedure used for the Q0837+109 data. Also shown in the figure as three solid lines are the averaged $1 + \xi_{pp}(\Delta v)$ and its 1-σ limits from a set of 400 simulated spectra. (b) The same as (a), but for the quasar Q1247+267 and the two redshifts $z = 2.039$ and $z = 1.674$.

Fig. 6. (a) $1 + \xi_{pp}$ as a function Δv for a $z_{em} = 3.326$ quasar. The open stars denote the measured pixel-pixel transmission correlation of Q0837+109. The three solid lines are the average and $\pm 1\sigma$ variation of 400 Model FB3 simulations. The rest of the lines show just the 400-simulation averages, for the following models: DB1 (dotted), FB1 (short-dashed), FB2 (long-dashed), FB4 (dot-short-dashed) and FB5 (dot-long-dashed). (b) Same as (a), but for a $z_{em} = 2.039$ quasar, Q1247+267.

Fig. 7 (a) Normalized flux or transmission as a function of the observed wavelength λ_{obs} for Q0837+109 (Sargent, Boksenberg & Steidel 1988). (b) Simulated spectrum using Model FB1 parameters and including noise. (c) A Model FB3 simulation with noise.

Fig. 8 Same as Fig.7(a,b,c), but for for the quasar Q1247+267.

Fig. 9. The influence of noise on the transmission correlation function. The open stars denote the measured $1 + \xi_{pp}$ of Q0837. Each curve shown is the average of a set of 400 simulated Model FB1 spectra. The solid line denotes the noise-free simulation. The dotted line is for $q_i\,\overline{n}_{con} = 100$ and $q_i\,\overline{n}_{sky} = 10$, the short-dashed is for $q_i\,\overline{n}_{con} = 25$ and $q_i\,\overline{n}_{sky} = 2.5$, and long-dashed line is for $q_i\,\overline{n}_{con} = 100$ and $q_i\,\overline{n}_{sky} = 100$.

Fig. 10. $\sigma(1 + \xi_{pp})$ as a function of Δv for a $z_{em} = 3.326$ quasar. Each curve shown is derived from a set of 400 simulated Model FB1 spectra. The solid is for the non-noisy simulations. The

dotted line is for $q_i \overline{n}_{con} = 100$ and $q_i \overline{n}_{sky} = 10$. The short-dashed line is for $q_i \overline{n}_{con} = 25$ and $q_i \overline{n}_{sky} = 2.5$. The long-dashed line is for $q_i \overline{n}_{con} = 100$ and $q_i \overline{n}_{sky} = 100$.

Fig. 11. (a) Comparison of $1 + \xi_{pp}(\Delta v)$ for 4 quasars (open stars) with simulations of Models FB1 (dashed lines) and FB3 (solid lines). The 3 lines show the mean $1 + \xi_{pp}$ and its $\pm 1\sigma$ variation, estimated from sets of 400 simulations. The quasars are (a) Q0424-131, (b) Q2206-199, (c) Q1511+091, (d) Q0014+813.

Fig. 12. The influence of the "proximity effect" on simulated quasar spectra for $z_{em} = 3.326$. Model FB1 parameters have been used. The first (top) panel is the spectrum without the proximity effect, which is the same realization as the Fig. 6(b) spectrum but without noise added. The second, third and fourth panels are the simulated spectra for the following values of $L_{31}h^2/J_{-21}$: 1 (second); 10 (third); and 100 (fourth). All 4 panels are derived from the same realization.

Fig. 13. The influence of the "proximity effect" on $1+\xi_{pp}$ as a function of Δv for $z_{em} = 3.326$. The open stars denote the results for the real spectrum of Q0837; the 3 solid lines are the mean $1+\xi_{pp}$ and its 1-σ limits from a set of 400 simulations using Model FB1 parameters and $L_{31}h^2/J_{-21} = 0$, *i.e.*, no proximity effect; the 3 long dashed lines are for $L_{31}h^2/J_{-21} = 1$; the three dotted lines are for $L_{31}h^2/J_{-21} = 10$; and the 3 short dashed lines are for $L_{31}h^2/J_{-21} = 100$.

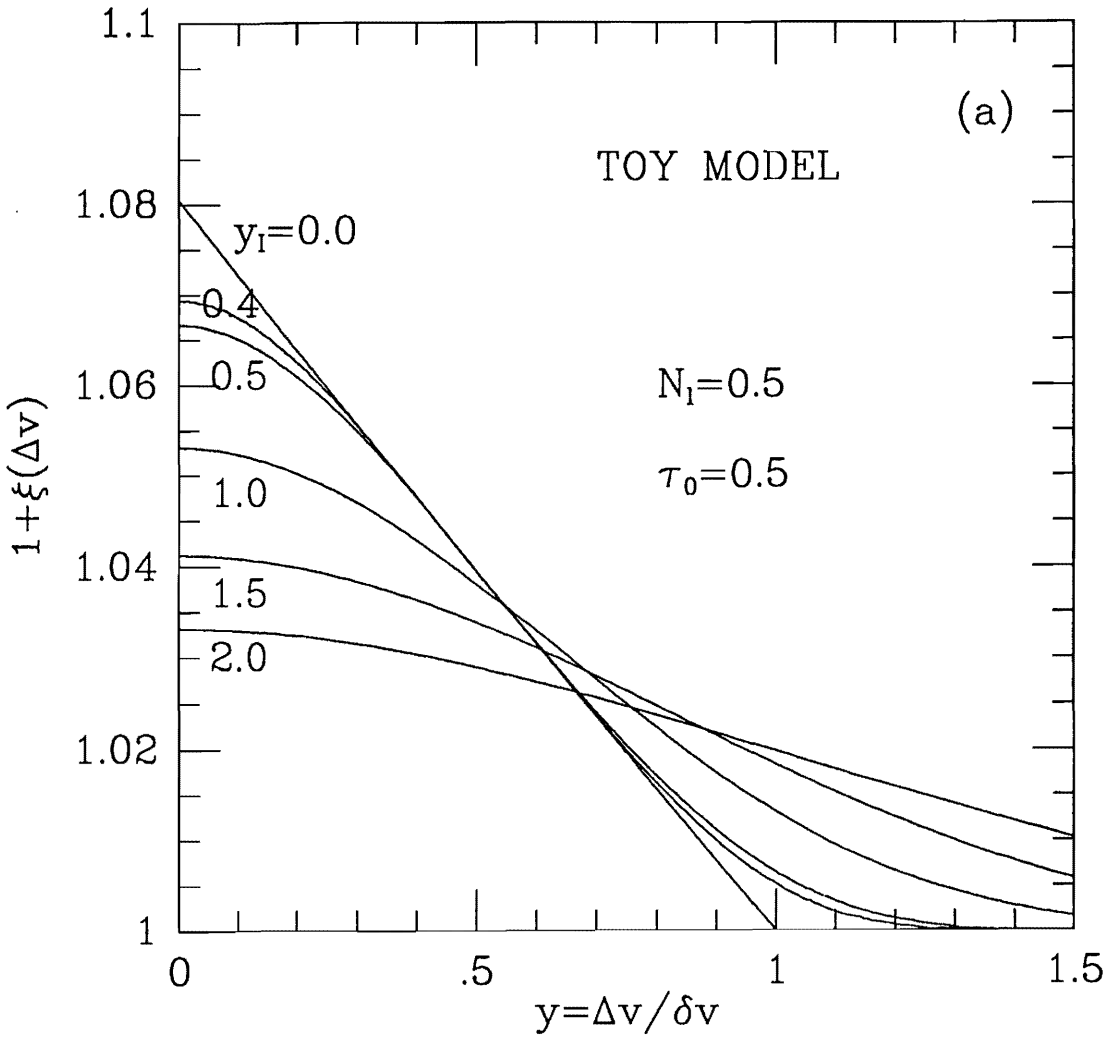
(a)
TOY MODEL
y_I=0.0
0.4
0.5
1.0
1.5
2.0
N_I=0.5
τ_0=0.5
1.1
1.08
1.06
1.04
1.02
1
0
.5
1
1.5
$1+\xi(\Delta v)$
$y=\Delta v/\delta v$

Fig. 1 (a)

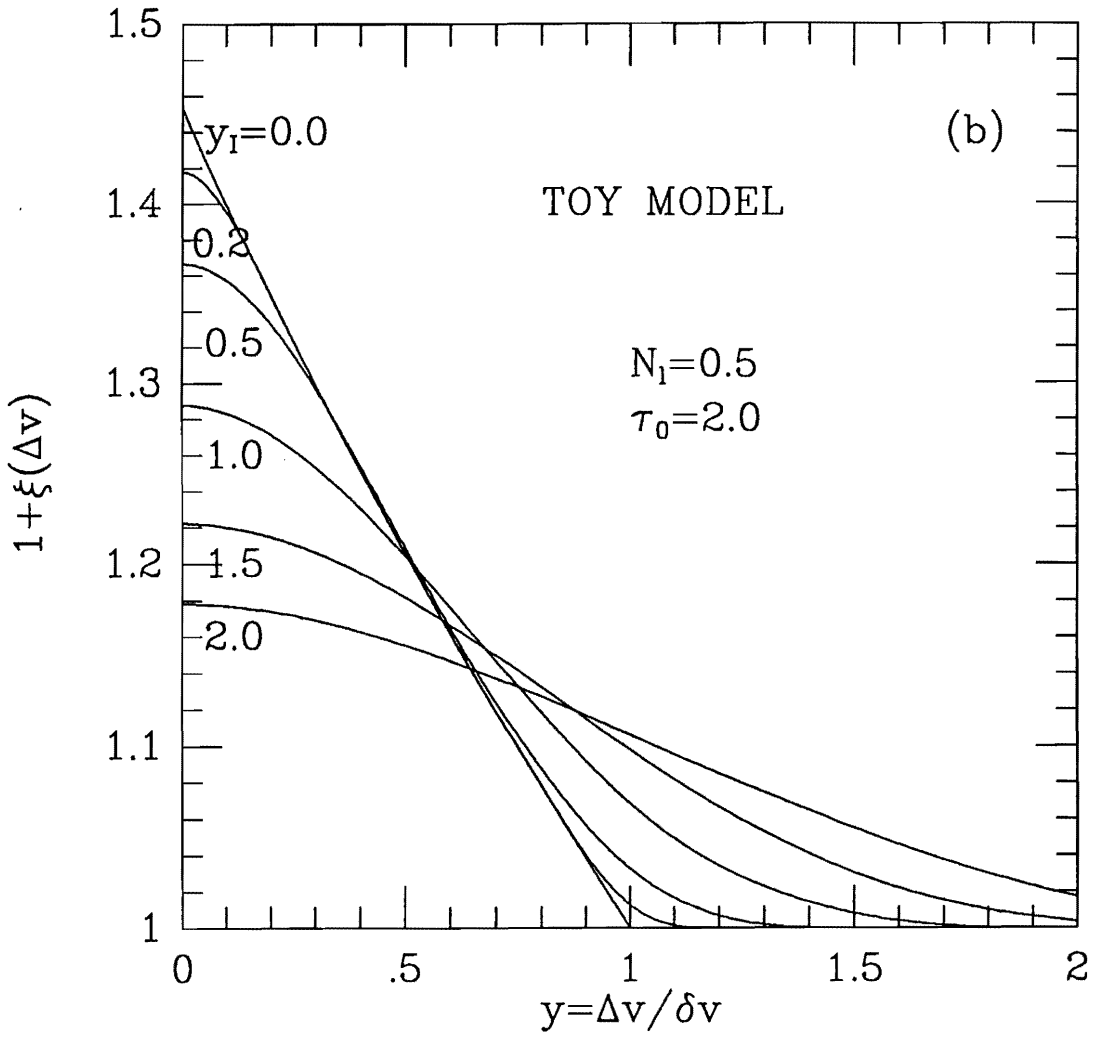
1.5
1.4
1.3
1.2
1.1
1
0
.5
1
1.5
2
$1+\xi(\Delta v)$
$y=\Delta v/\delta v$
y_I=0.0
0.2
0.5
1.0
1.5
2.0
(b)
TOY MODEL
N_I=0.5
τ_0=2.0

Fig. 1 (b)

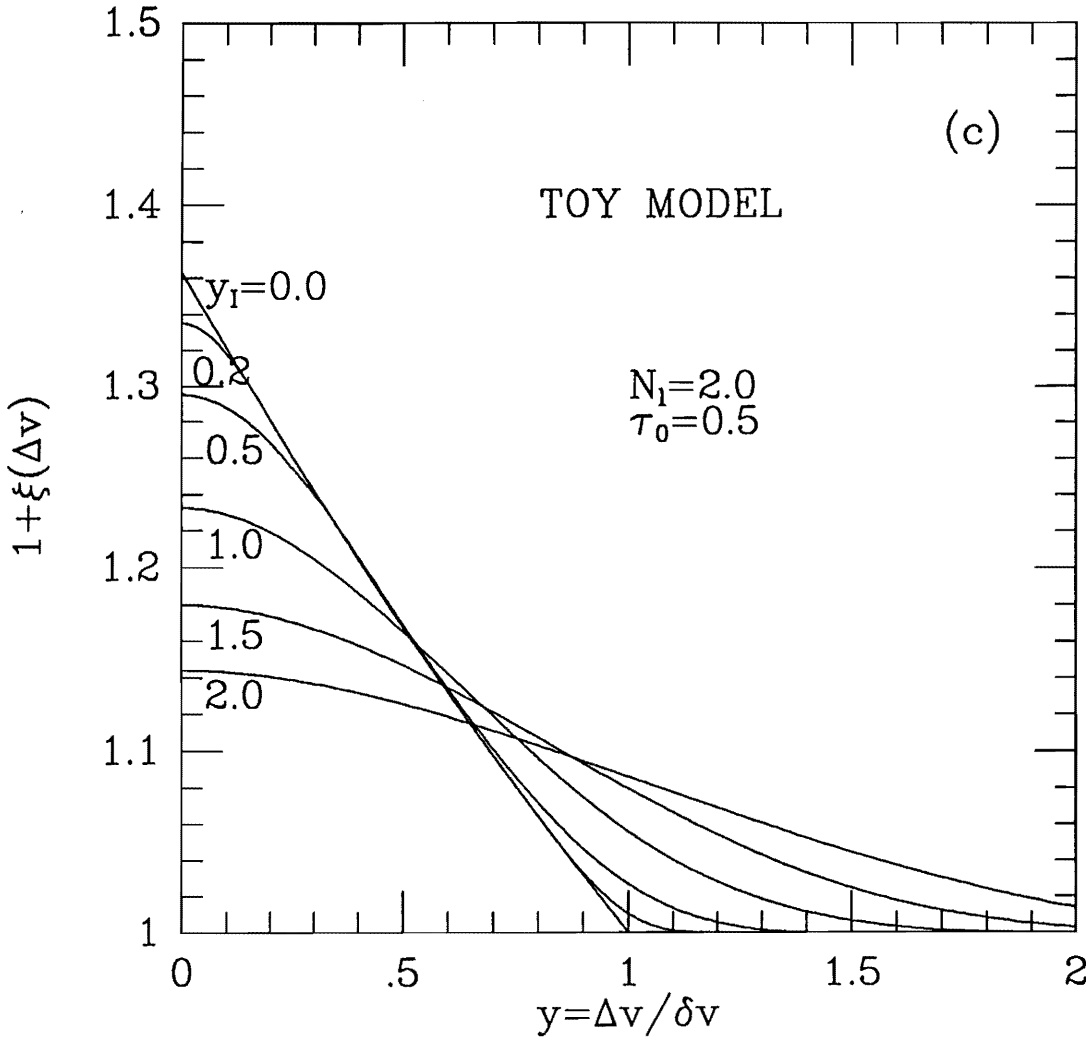
(c)
TOY MODEL
y_I=0.0
0.2
0.5
1.0
1.5
2.0
N_1=2.0
τ_0=0.5
1+ξ(Δv)
y=Δv/δv
1.5
1.4
1.3
1.2
1.1
1
0
.5
1
1.5
2

Fig. 1(c)

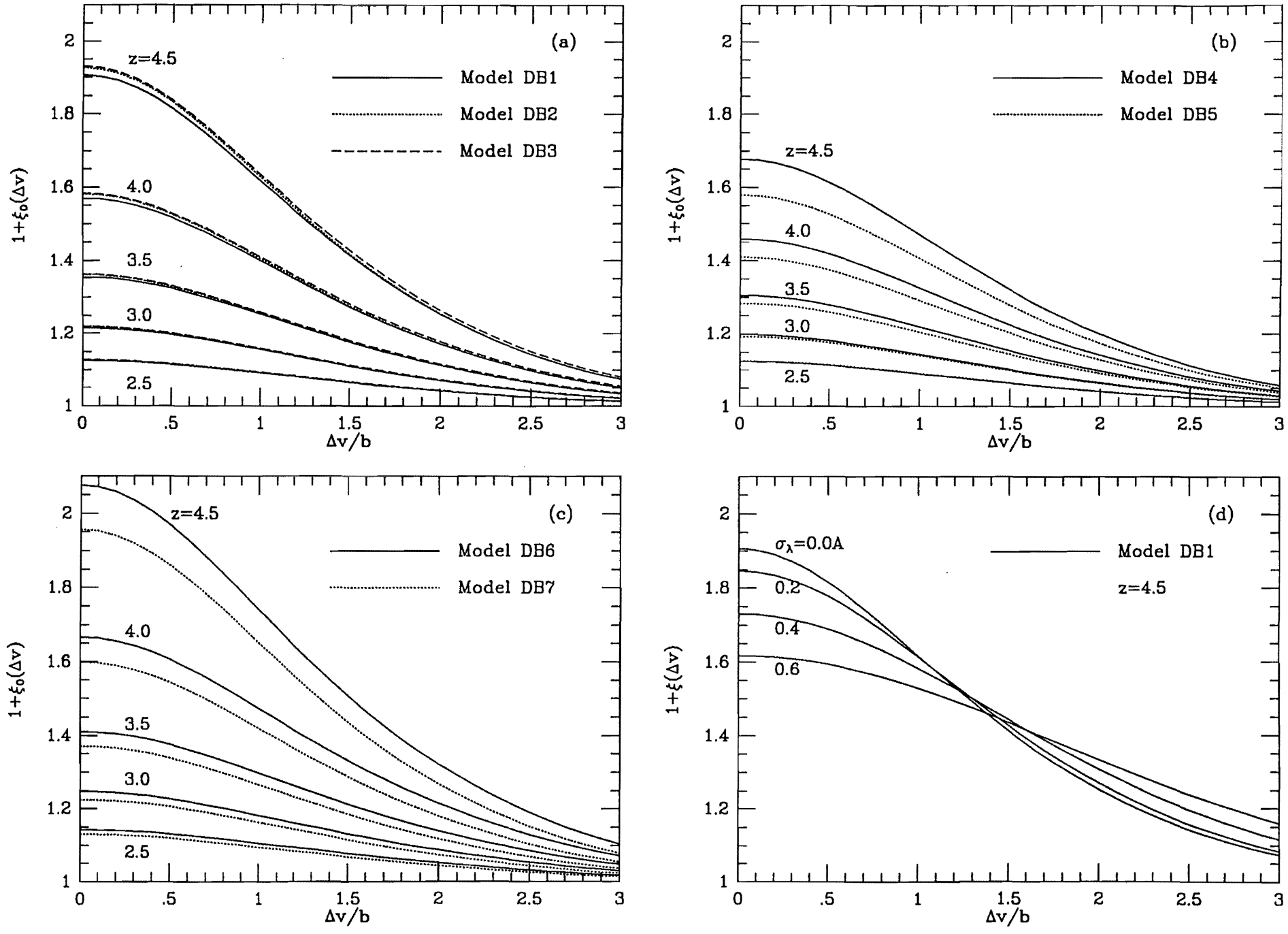
(a)
z=4.5
4.0
3.5
3.0
2.5
Model DB1
Model DB2
Model DB3
1+ξ₀(Δv)
Δv/b
(b)
Model DB4
Model DB5
(c)
Model DB6
Model DB7
(d)
σλ=0.0A
0.2
0.4
0.6
Model DB1
z=4.5
1+ξ(Δv)

Fig. 2

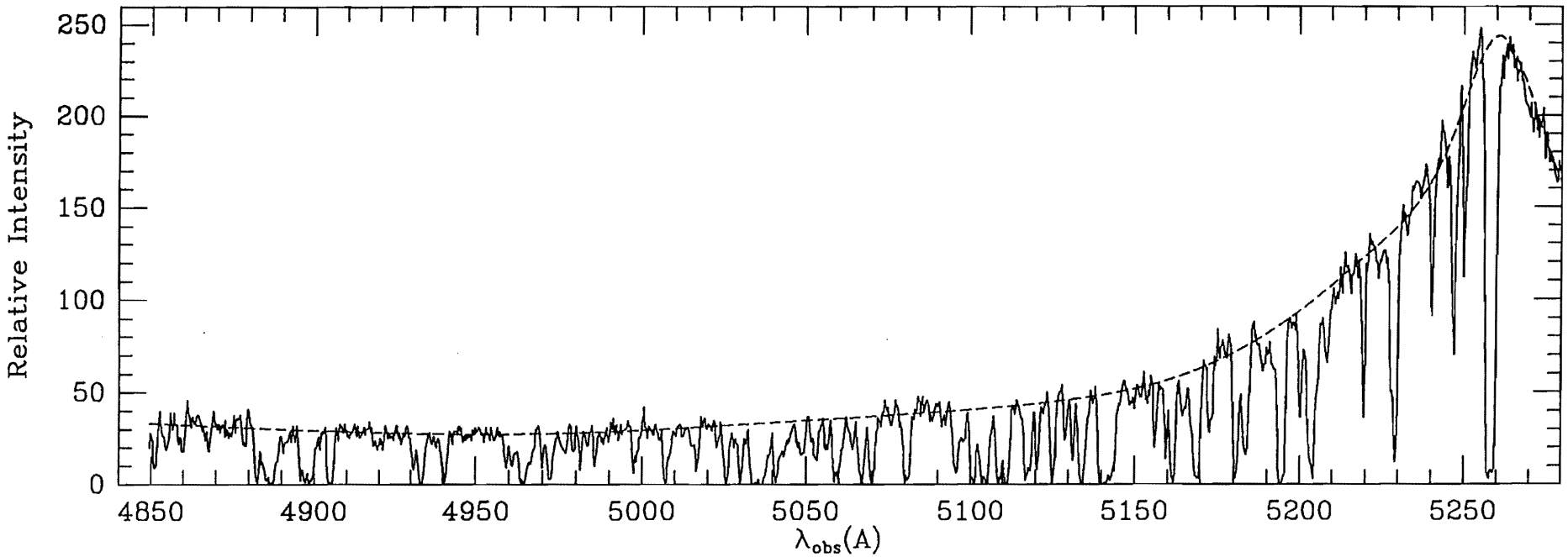
Relative Intensity
250
200
150
100
50
0
4850
4900
4950
5000
5050
5100
5150
5200
5250
λ_{obs}(A)

Fig. 3

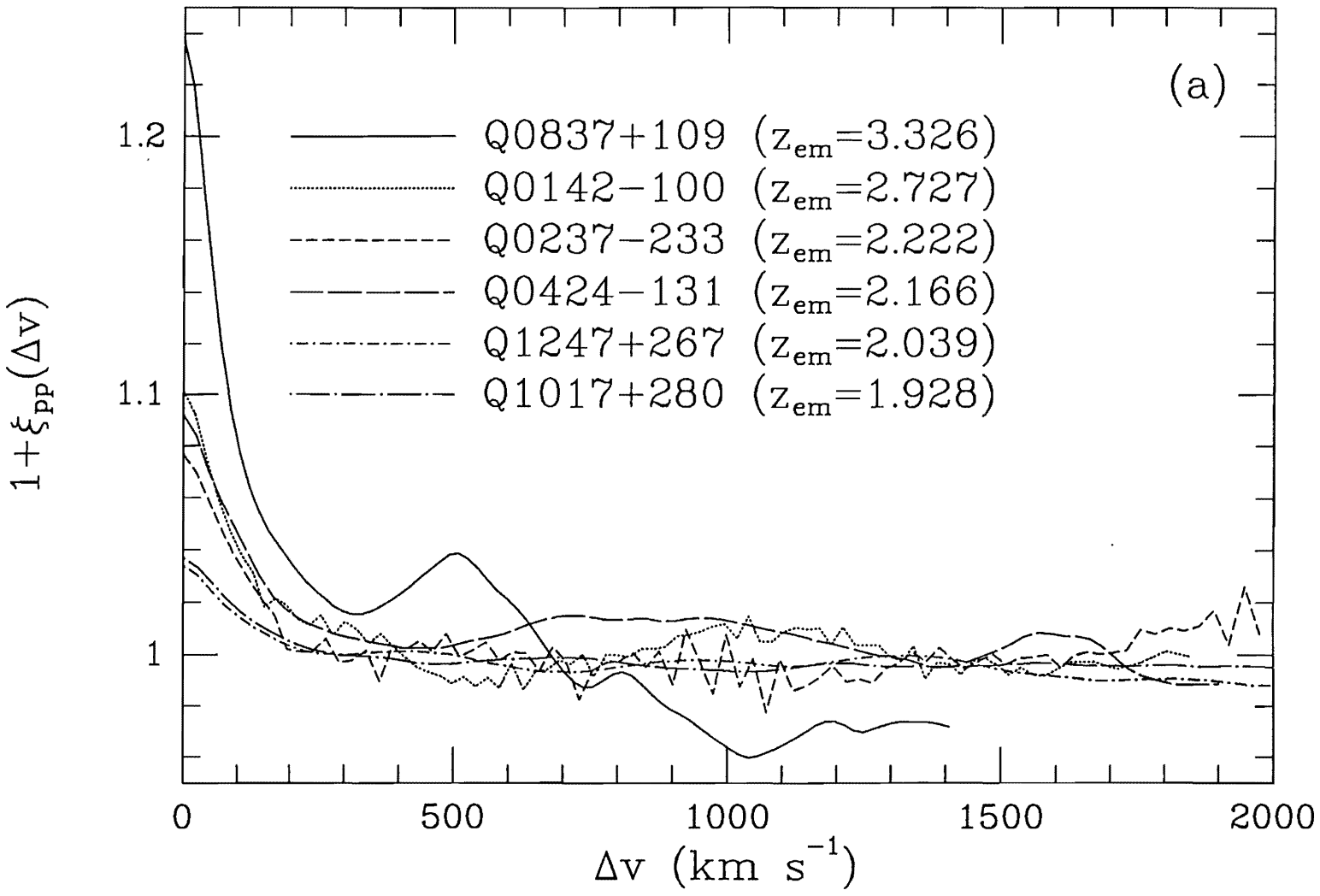
(a)
Q0837+109 (z_{em}=3.326)
Q0142−100 (z_{em}=2.727)
Q0237−233 (z_{em}=2.222)
Q0424−131 (z_{em}=2.166)
Q1247+267 (z_{em}=2.039)
Q1017+280 (z_{em}=1.928)
1.2
1.1
1
0
500
1000
1500
2000
$1+\xi_{pp}(\Delta v)$
Δv (km s^{-1})

Fig. 4 (a)

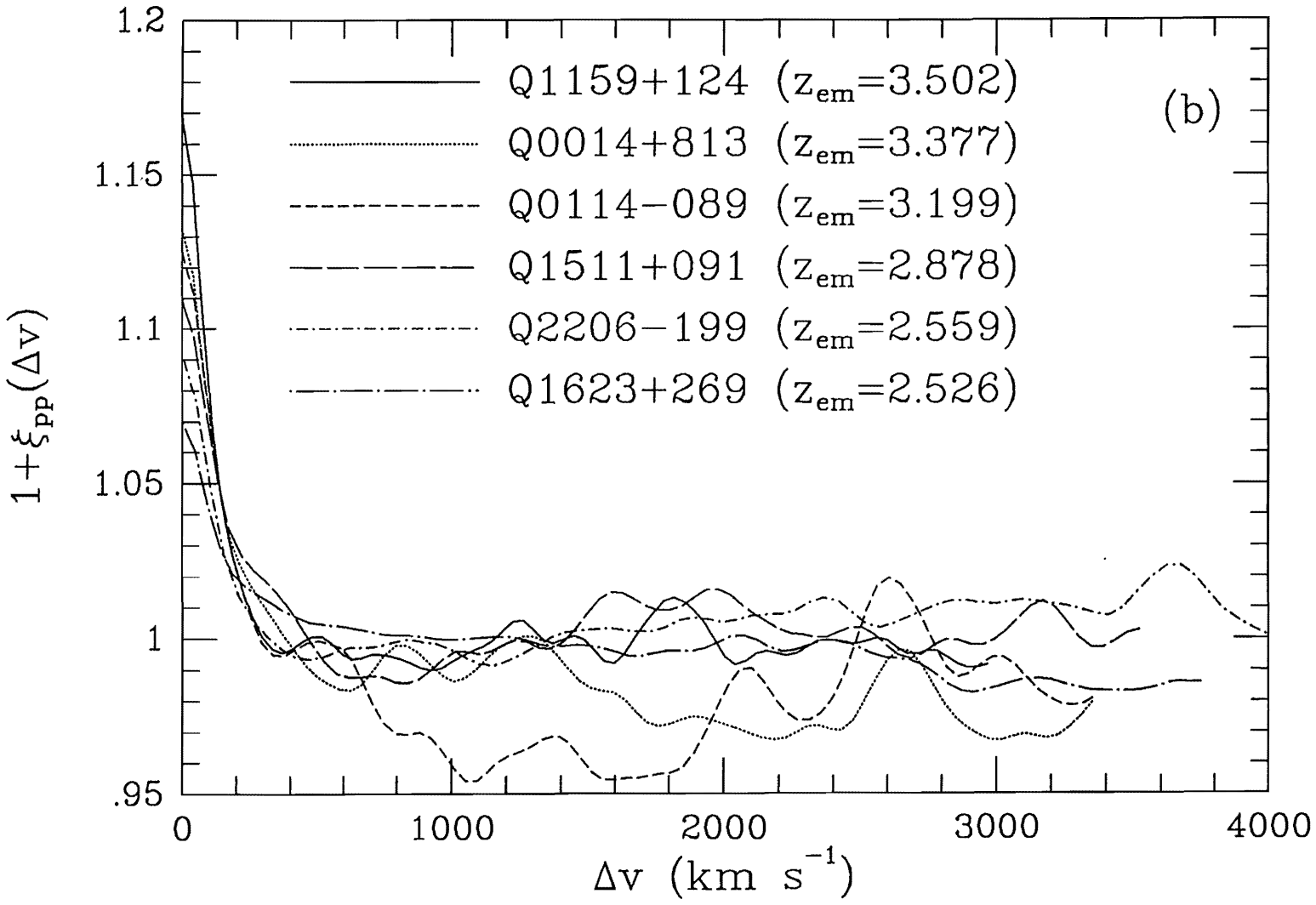
Q1159+124 (z_{em}=3.502)
Q0014+813 (z_{em}=3.377)
Q0114−089 (z_{em}=3.199)
Q1511+091 (z_{em}=2.878)
Q2206−199 (z_{em}=2.559)
Q1623+269 (z_{em}=2.526)
(b)
1.2
1.15
1.1
1.05
1
.95
0
1000
2000
3000
4000
$1+\xi_{pp}(\Delta v)$
Δv (km s^{-1})

Fig. 4(b)

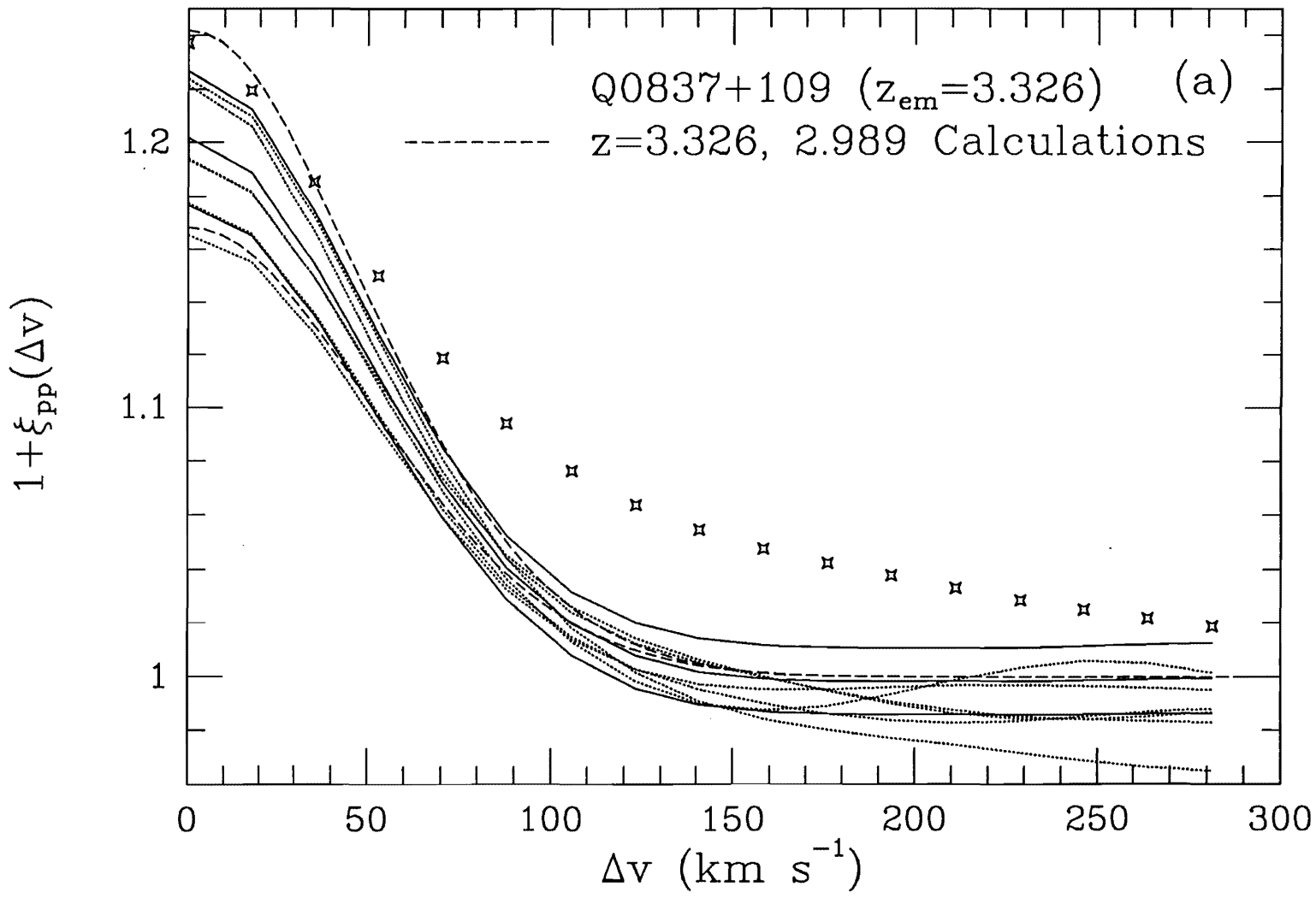
Q0837+109 (z_{em}=3.326) (a)
z=3.326, 2.989 Calculations
1.2
1.1
1
0
50
100
150
200
250
300
$1+\xi_{pp}(\Delta v)$
Δv (km s^{-1})

Fig. 5 (a)

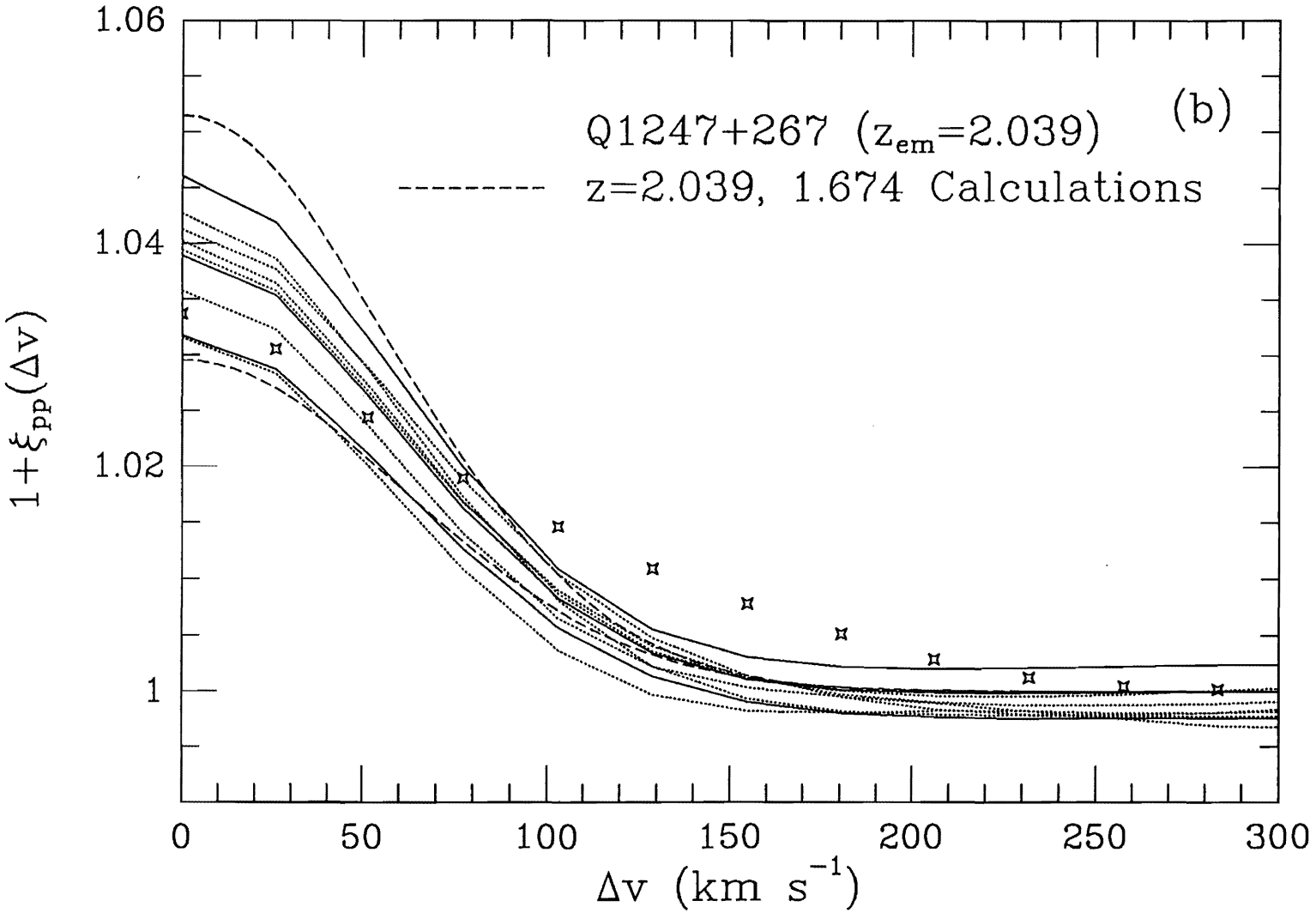
1.06
1.04
1.02
1
0
50
100
150
200
250
300
$1+\xi_{pp}(\Delta v)$
Δv (km s^{-1})
Q1247+267 (z_{em}=2.039)
(b)
z=2.039, 1.674 Calculations

Fig. 5(b)

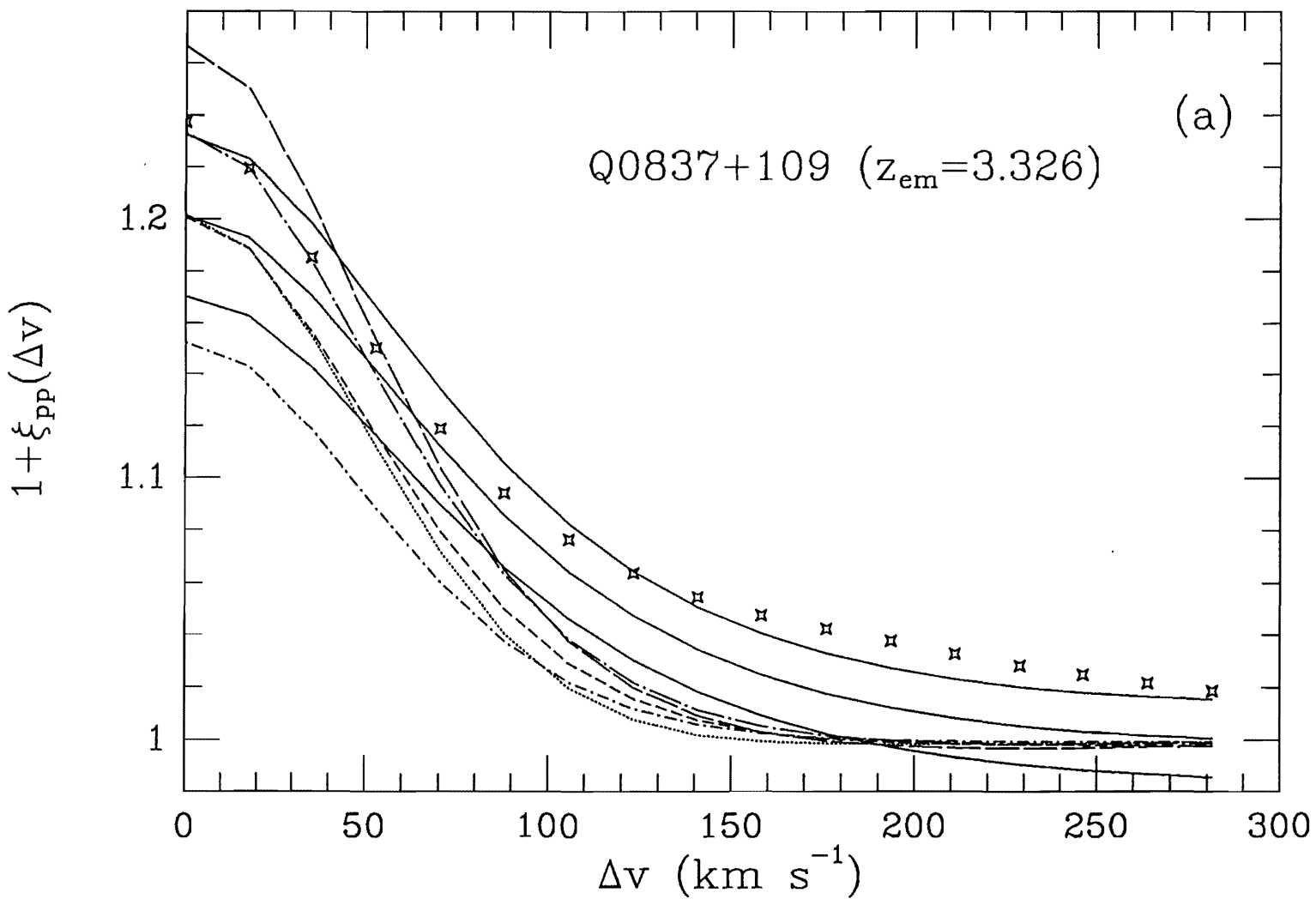
(a)
Q0837+109 (z_{em}=3.326)
1.2
1.1
1
0
50
100
150
200
250
300
$1+\xi_{pp}(\Delta v)$
Δv (km s^{-1})

Fig. 6(a)

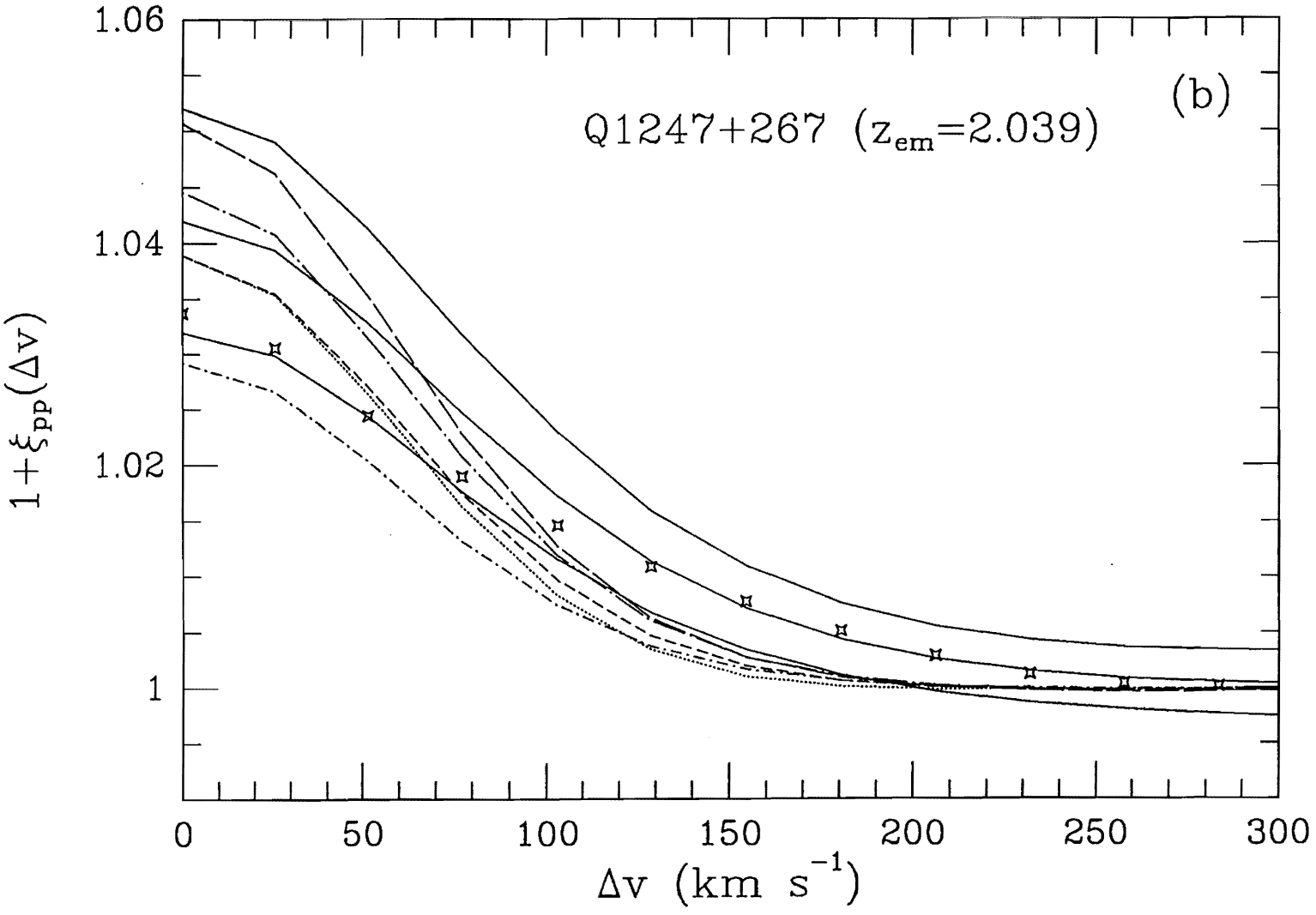
(b)
Q1247+267 (z_{em}=2.039)
1.06
1.04
1.02
1
0
50
100
150
200
250
300
$1+\xi_{pp}(\Delta v)$
Δv (km s^{-1})

Fig. 6(b)

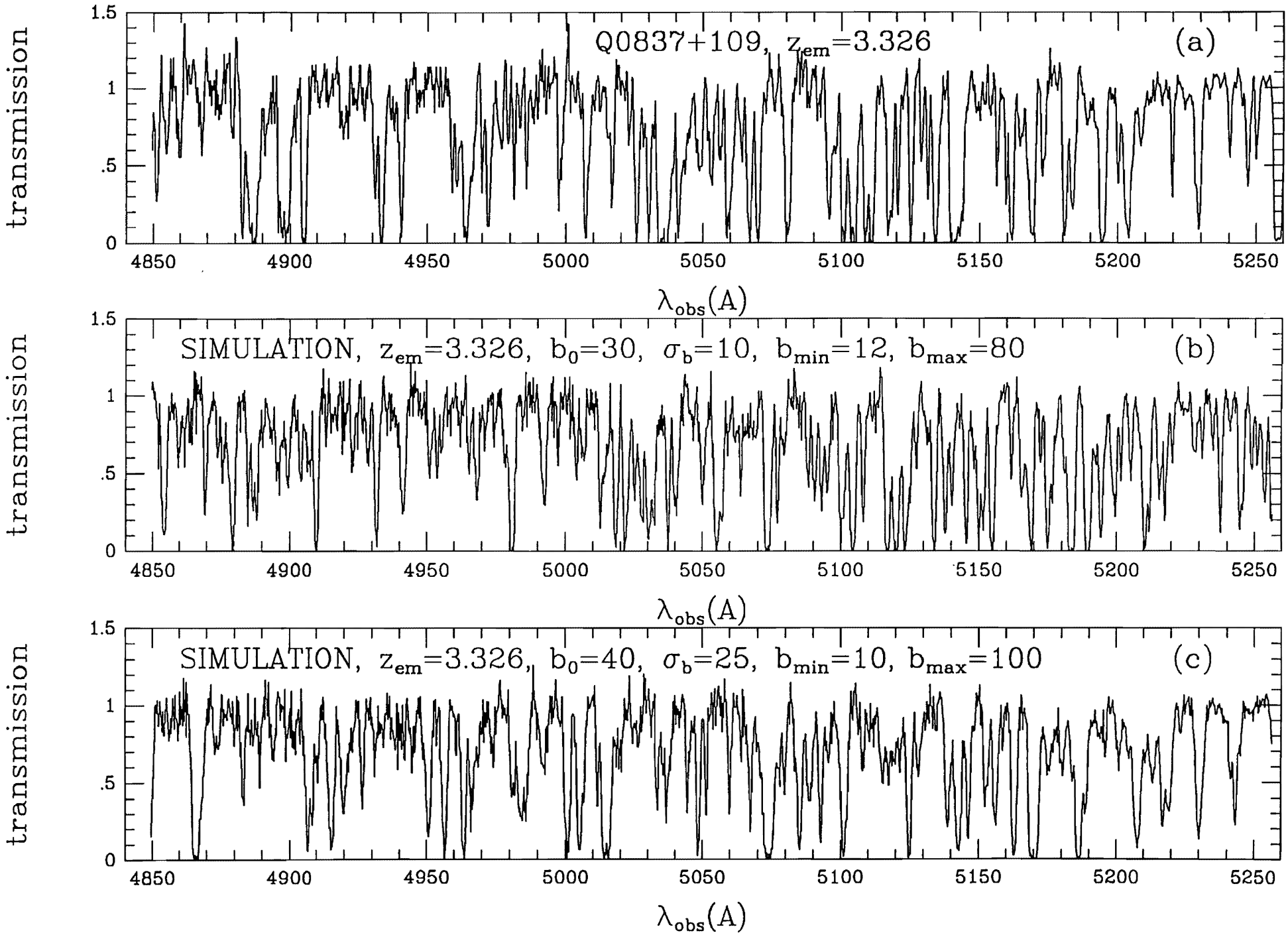
Q0837+109, z_{em}=3.326
(a)
SIMULATION, z_{em}=3.326, b_0=30, σ_b=10, b_{min}=12, b_{max}=80
(b)
SIMULATION, z_{em}=3.326, b_0=40, σ_b=25, b_{min}=10, b_{max}=100
(c)
transmission
λ_{obs}(A)
1.5
1
.5
0
4850
4900
4950
5000
5050
5100
5150
5200
5250

Fig. 7

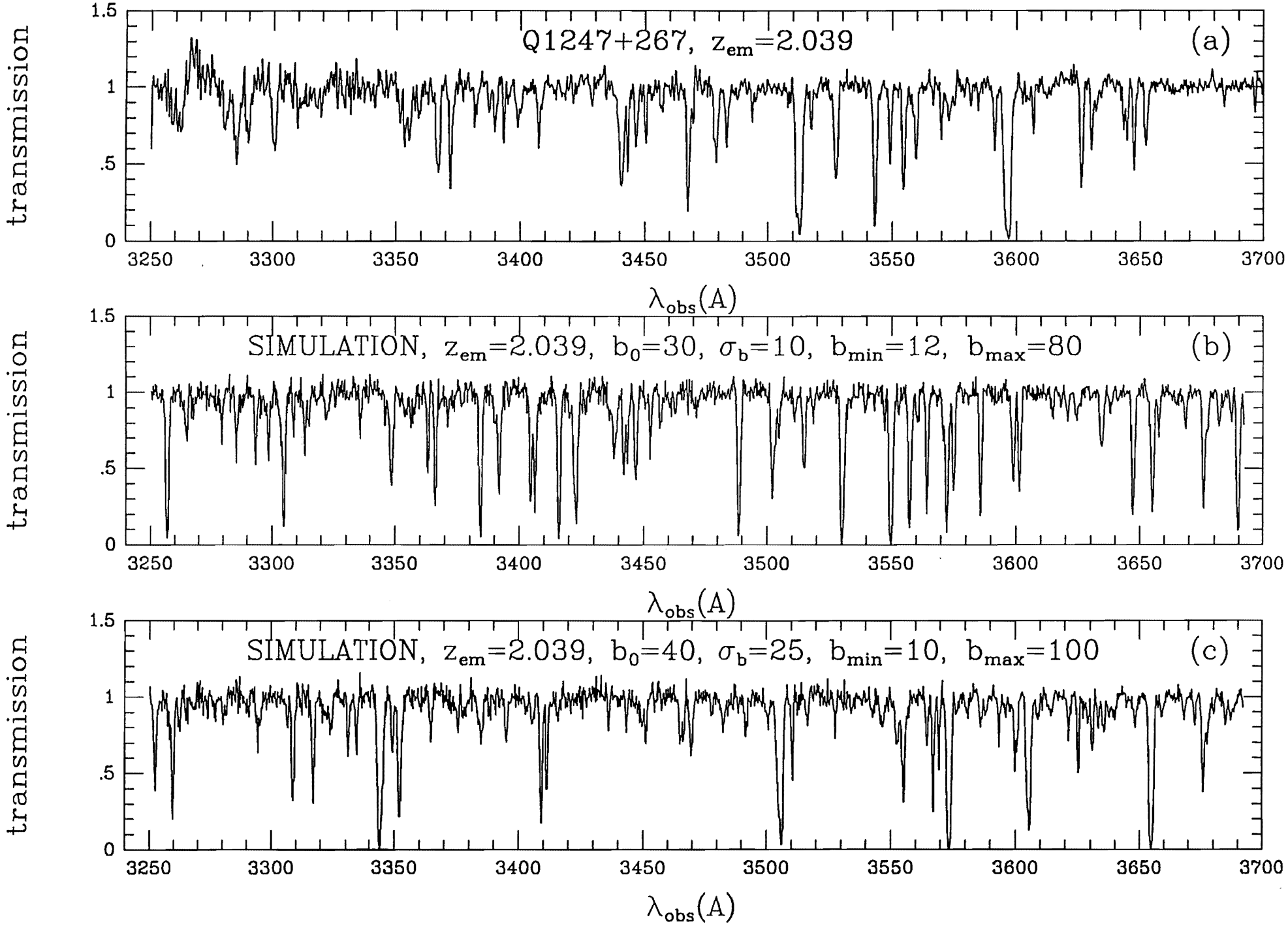
Q1247+267, z_{em}=2.039
(a)
SIMULATION, z_{em}=2.039, b_0=30, σ_b=10, b_{min}=12, b_{max}=80
(b)
SIMULATION, z_{em}=2.039, b_0=40, σ_b=25, b_{min}=10, b_{max}=100
(c)
transmission
λ_{obs}(A)
1.5
1
.5
0
3250
3300
3350
3400
3450
3500
3550
3600
3650
3700

Fig. 8

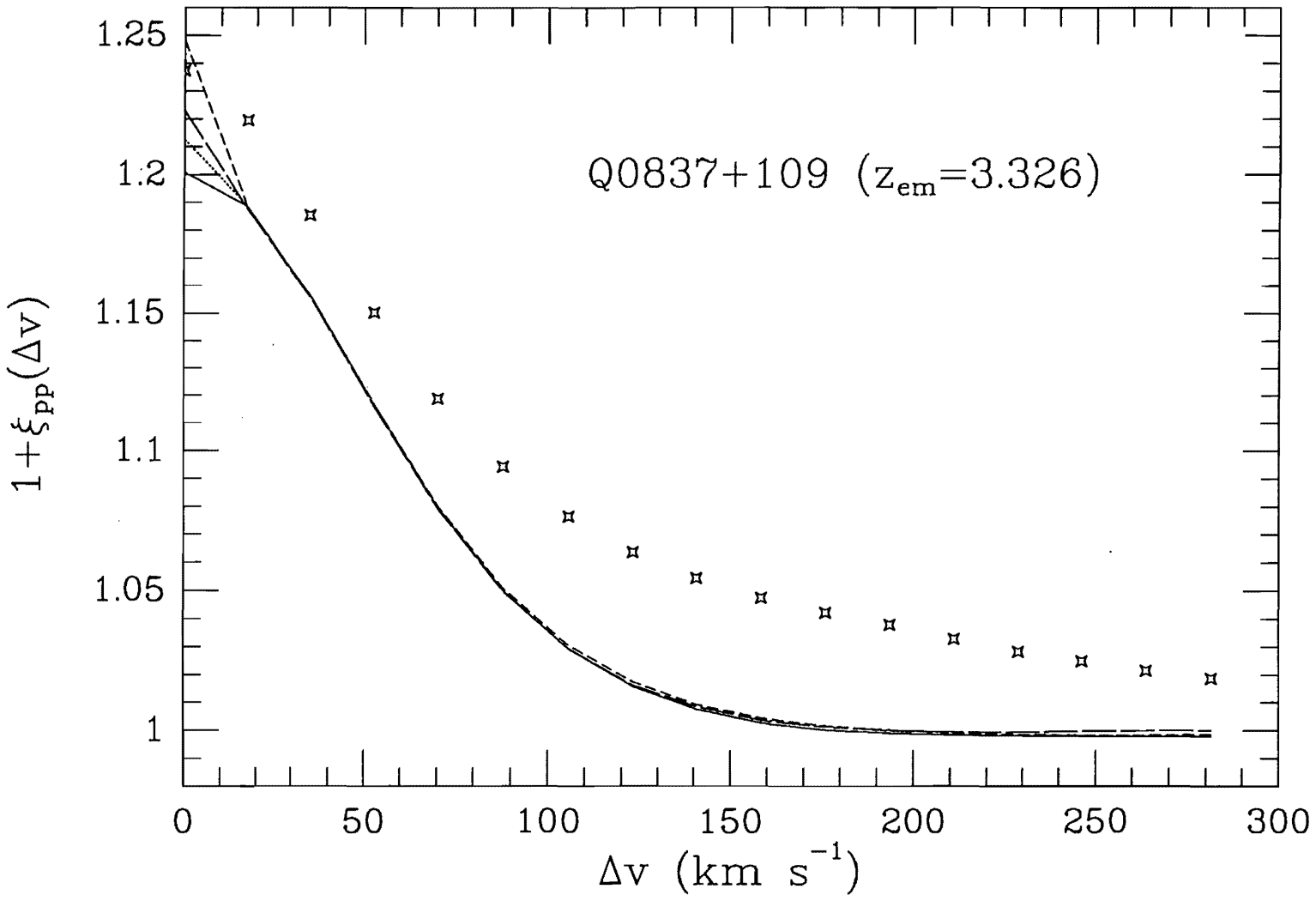
Q0837+109 (z_{em}=3.326)
1.25
1.2
1.15
1.1
1.05
1
0
50
100
150
200
250
300
$1+\xi_{pp}(\Delta v)$
Δv (km s^{-1})

Fig. 9

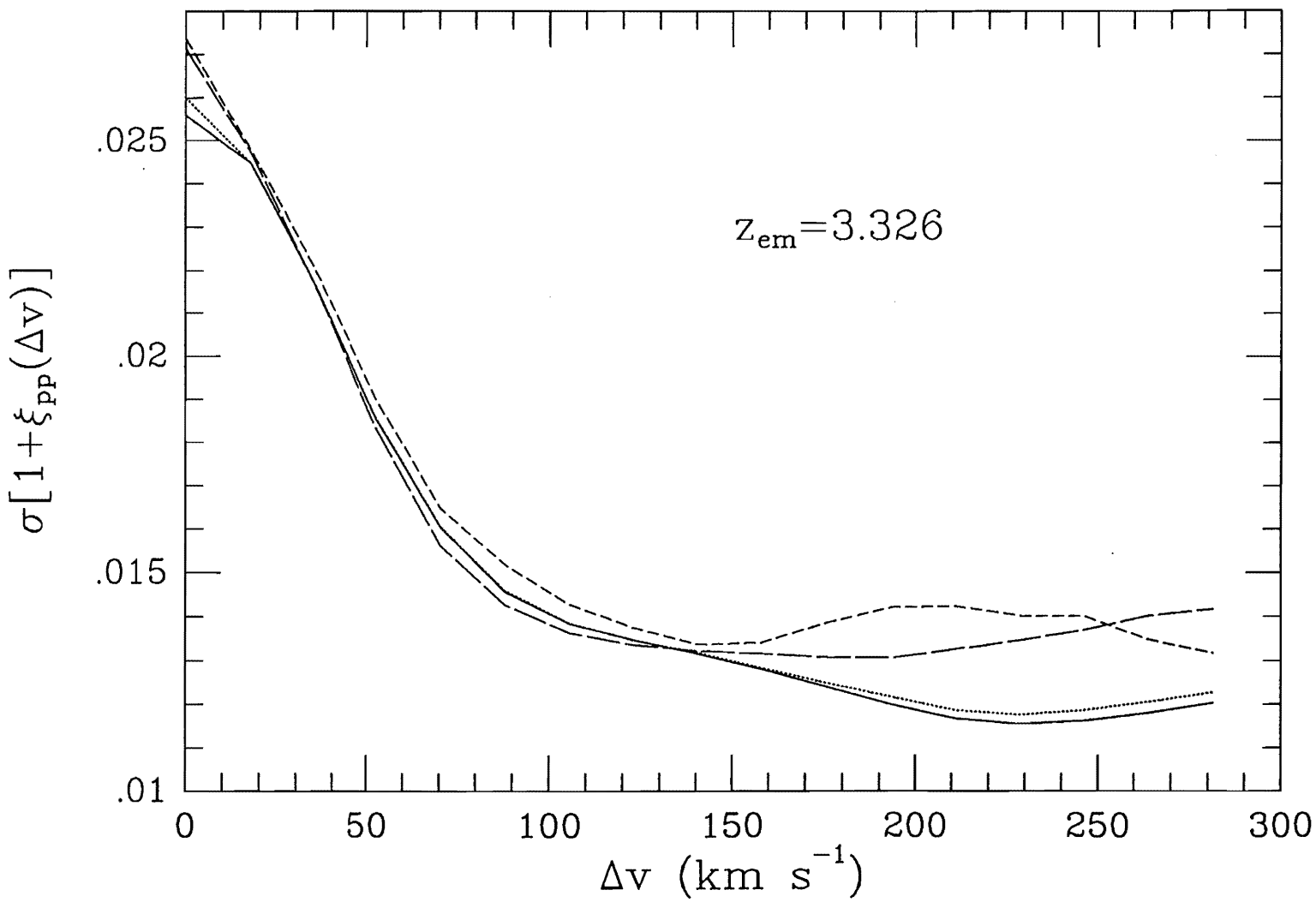
z_{em}=3.326
.025
.02
.015
.01
0
50
100
150
200
250
300
$\sigma[1+\xi_{pp}(\Delta v)]$
Δv (km s^{-1})

Fig. 10

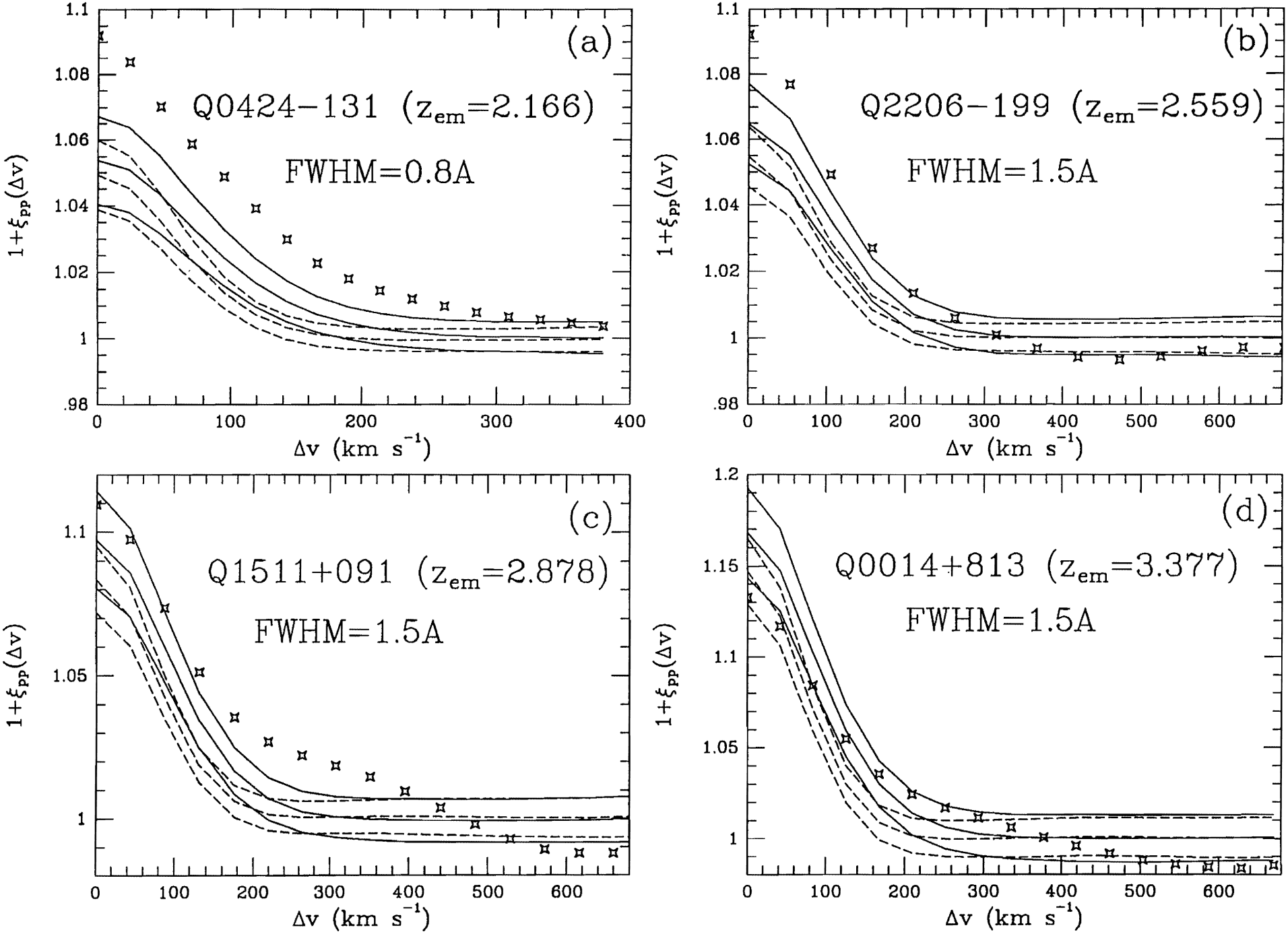
(a)
Q0424−131 (z_{em}=2.166)
FWHM=0.8A
(b)
Q2206−199 (z_{em}=2.559)
FWHM=1.5A
(c)
Q1511+091 (z_{em}=2.878)
FWHM=1.5A
(d)
Q0014+813 (z_{em}=3.377)
FWHM=1.5A
$1+\xi_{pp}(\Delta v)$
Δv (km s^{-1})

Fig. 11

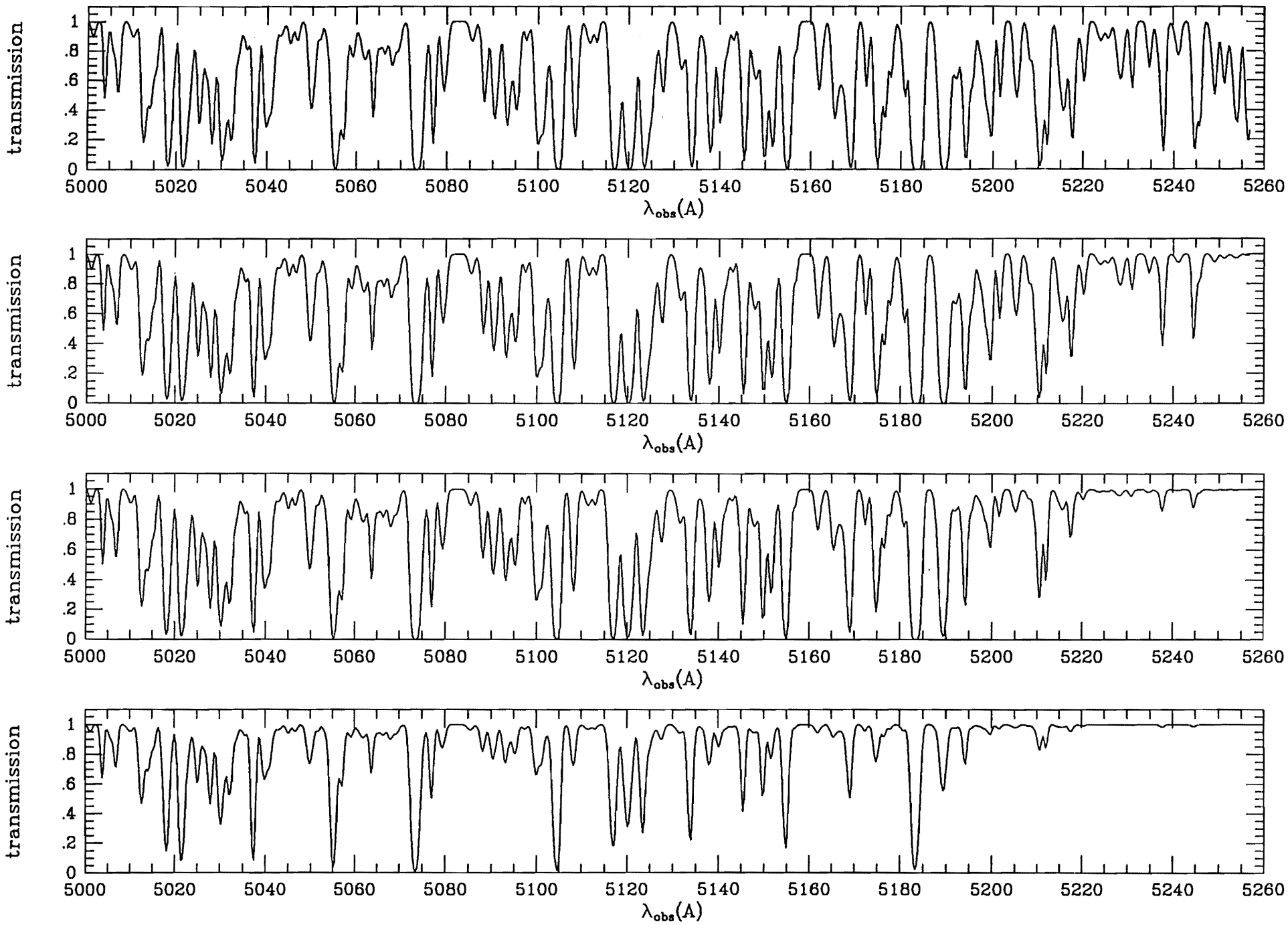
transmission
1
.8
.6
.4
.2
0
5000
5020
5040
5060
5080
5100
5120
5140
5160
5180
5200
5220
5240
5260
λ_{obs}(A)

Fig. 12

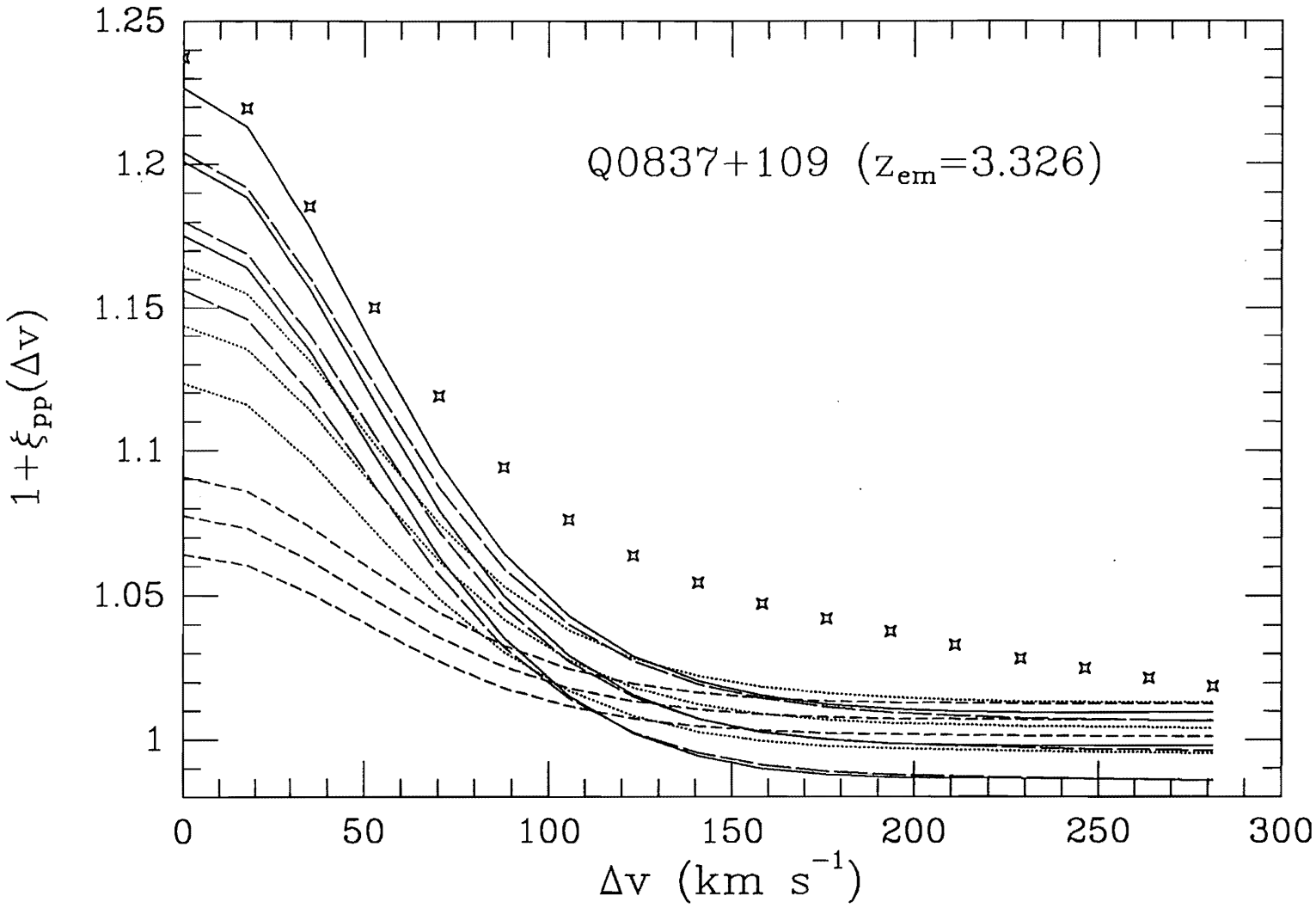
Q0837+109 (z_{em}=3.326)
$1+\xi_{pp}(\Delta v)$
Δv (km s^{-1})
1.25
1.2
1.15
1.1
1.05
1
0
50
100
150
200
250
300

Fig. 13